



저작자표시-비영리-변경금지 2.0 대한민국

이용자는 아래의 조건을 따르는 경우에 한하여 자유롭게

- 이 저작물을 복제, 배포, 전송, 전시, 공연 및 방송할 수 있습니다.

다음과 같은 조건을 따라야 합니다:



저작자표시. 귀하는 원저작자를 표시하여야 합니다.



비영리. 귀하는 이 저작물을 영리 목적으로 이용할 수 없습니다.



변경금지. 귀하는 이 저작물을 개작, 변형 또는 가공할 수 없습니다.

- 귀하는, 이 저작물의 재이용이나 배포의 경우, 이 저작물에 적용된 이용허락조건을 명확하게 나타내어야 합니다.
- 저작권자로부터 별도의 허가를 받으면 이러한 조건들은 적용되지 않습니다.

저작권법에 따른 이용자의 권리는 위의 내용에 의하여 영향을 받지 않습니다.

이것은 [이용허락규약\(Legal Code\)](#)을 이해하기 쉽게 요약한 것입니다.

[Disclaimer](#)

공학박사 학위논문

**Study on Formation and Decomposition
of Perovskite Crystals for High Efficiency
and Stability**

고효율 및 고안정성 태양전지 개발을 위한
페로브스카이트 결정 형성 및 분해 연구

2018년 2월

서울대학교 대학원

기계항공공학부

안 남 영

고효율 및 고안정성 태양전지 개발을 위한
페로브스카이트 결정 형성 및 분해 연구
Study on Formation and Decomposition of Perovskite
Crystals for High Efficiency and Stability

지도교수 최 만 수

이 논문을 공학박사 학위논문으로 제출함

2017년 11월


서울대학교 대학원

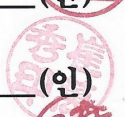
기계항공공학부


안 남 영


안남영의 공학박사 학위논문을 인준함


2017년 12월

위원장 : 전 누리 (인) 

부위원장 : 최 만 수 (인) 

위원 : 이 훈 석 (인) 

위원 : 성 영 은 (인) 

위원 : 고 민 재 (인) 

Study on Formation and Decomposition of Perovskite Crystals for High Efficiency and Stability

Namyoung Ahn

School of Mechanical and Aerospace Engineering

The Graduate School

Seoul National University

Abstract

Organic inorganic hybrid perovskite crystals, which can be easily formed by chemical reaction of metal halide and organic halide, show excellent photo-electronic properties such as band gap, absorption coefficient, and carrier diffusion length by themselves. The properties are dependent on comprehensive quality of perovskite crystal-clustered thin films which finally influences on photovoltaic performance of complete devices. To realize perovskite solar cells with high performance, it is required to understand fundamental principles of crystal formation and develop fabrication process of perovskite crystal-clustered thin films based on basic principles. Additionally, since these perovskites have weak bonding

between organic and inorganic parts, the decomposition of perovskites occurs actively in air condition under light irradiation. To achieve stable operation of perovskite solar cells for several years, investigation of fundamental origin and principle of perovskite decomposition should be preferentially performed.

First, the general way to fabricate perovskite films is reacting solidified lead halide thin films with organic halide dissolved in solutions. In this crystallization process, which is simply called two-step method, various reaction conditions affect the crystallization growth rate and crystal sizes which consequently determine the quality of perovskite films. To obtain high-quality perovskite films, the effect of reaction conditions such as temperature and concentration of organic halide was theoretically and experimentally investigated. Based on thermodynamic analysis on the crystallization of perovskite, the grain size equation was derived by considering the change in Gibbs free energy. From the equation, the grain sizes of the perovskite can be controlled not only by organic halide concentration but also by the reaction temperature of the crystallization process. By varying the reaction temperature from $-10\text{ }^{\circ}\text{C}$ to $50\text{ }^{\circ}\text{C}$, the grain sizes were dramatically changed from few hundred nanometers to few micrometers under the same concentration. It is found that the concentration and the temperature play a critical role in determining the grain sizes and the performance of perovskite device.

In the two-step method, there is the limitation in terms of perovskite film coverage due to crystal growth along vertical direction. Since the

perovskite coverage is crucial in photovoltaic performance, it is required to develop a new fabrication method which enables formation of fully-covered, dense and homogeneous perovskite films by controlling the perovskite crystallization. Before the formation of perovskite films, transparent Lewis-base adduct films was previously formed as the intermediate step and heated to be slowly crystallized by removing Lewis-base. Perovskites fabricated from Lewis-base adduct exhibited high charge extraction characteristics and slow recombination rate. Finally, Perovskite solar cells fabricated via Lewis-base adduct approach showed the best PCE of 19.7% and average PCE of 18.3% from 41 cells, which is indicative of high reproducibility.

These perovskite materials are vulnerable to the deterioration caused by humidity and light. The most widely used perovskite, $\text{CH}_3\text{NH}_3\text{PbI}_3$, is structurally distorted tetragonal crystals due to unbalance of ionic radii between ions. The crystal structure of perovskites can become more stable by increasing the Goldschmidt tolerance factor close to unity by incorporating other organic cation and halide anion with different ion sizes. An addition of formamidinium ($\text{HC}(\text{NH}_2)_2$) cation and bromide (Br) anion not only structurally stabilize the perovskite materials by inducing cubic crystals, but also enhance their photovoltaic performance. By comprehensively optimizing mixed cation and/or halide anion system of $\text{MA}_x\text{FA}_{1-x}\text{PbI}_y\text{Br}_{3-y}$ in terms of both stability and performance, structurally-stabilized mixed compositional $\text{MA}_{0.6}\text{FA}_{0.4}\text{PbI}_{2.9}\text{Br}_{0.1}$ perovskite-based devices formed via lewis-base adduct method exhibited the best PCE of

20.2% without photocurrent hysteresis and enhanced stability under one sun illumination.

Perovskite solar cells have shown fast degradation under actual operation even with encapsulation and its reason has been still elusive. A novel experimental set-up to deposit charges generated via a corona discharger on the perovskite surface reveals that perovskite materials degrade irreversibly through grain boundaries in the presence of moisture only when charges traps on the perovskite surface. These results indicate that the moisture-induced irreversible decomposition of perovskite materials was triggered by trapped charges. The Kelvin Probe Force Microscopy measurements confirmed that charges are trapped preferentially on the grain boundaries when gas ions are deposited and light is illuminated. Moreover, the synergetic effect of oxygen on the trapped-charge driven degradation was also identified. From these observations, possible scenario on the degradation mechanism is suggested. The deprotonation of organic cation induced by locally-intensified electrostatic force due to trapped charge would be attributed to the irreversible degradation of perovskite materials.

Keywords: perovskite solar cell, Gibbs free energy, grain size equation, lewis base adduct, tolerance factor, cubic structure, mixed compositional perovskite, degradation mechanism, trapped charge

Student Number: 2013-23832

Contents

Abstract	ii
Contents	vi
List of Tables	x
Nomenclature	xi
List of Figures	xv
Chapter 1. Introduction	1
1.1. Research Background.....	1
1.2. Thesis Outline	10
Chapter 2. Thermodynamic Regulation of Perovskite (CH₃NH₃PbI₃) Crystal Growth	11
2.1. Introduction	11
2.2. Results and Discussion.....	13
2.3. Conclusions	30
2.4. Experimental methods.....	31
Chapter 3. Lewis-base Adduct Assisted Perovskite Crystal Growth for High Performance	34
3.1. Introduction	34
3.2. Results and Discussion.....	36
3.3. Conclusions	56
3.4. Experimental methods.....	57
Chapter 4. Compositional Perovskite Systems with	

Cubic Structure for Long-Term Stability	62
4.1. Introduction	62
4.2. Results and Discussion.....	64
4.3. Conclusions	75
4.4. Experimental methods.....	76
Chapter 5. Trapped-Charge Driven Degradation of Perovskite Solar Cells	78
5.1. Introduction	78
5.2. Results and Discussion.....	81
5.3. Conclusions	109
5.4. Experimental methods.....	110
Chapter 6. References.....	114
Abstract (in Korean).....	121
List of Publications	125

List of Tables

Table 2.1 Grain sizes, short-circuit photocurrent density (J_{sc}), open-circuit voltage (V_{oc}), fill factor (FF) and power conversion efficiency (PCE) versus MAPbI ₃ concentration.....	21
Table 2.2 Short-circuit photocurrent density (J_{sc}), open-circuit voltage (V_{oc}), fill factor (FF) and power conversion efficiency (PCE) depending on reaction temperature. The data represent the best performing device for each reaction temperature.....	26
Table 3.1 Stretching frequency of S=O for liquid DMSO and powdered PbI ₂ •DMSO and MAI•PbI ₂ •DMSO adducts, along with their chemical structures.....	43
Table 3.2 Parameters for photo-CELIV measurements.....	47
Table 3.3 Standard deviation of photovoltaic parameters and power conversion efficiency (PCE) for 41 perovskite solar cells based on the adduct-induced MAPbI ₃ . Average J_{sc} , V_{oc} , FF and PCE were 23.44 mA/cm ² , 1.070 V, 0.729 and 18.30%, respectively..	53
Table 5.1 The parameters for ion generation and data obtained from MFC controller and Faradaycup.....	112

Nomenclature

G_v	Gibbs free energy per unit volume	[J m ⁻³]
G_s	Gibbs free energy per unit area	[J m ⁻²]
k	Boltzmann constant	[J K ⁻¹]
T	Temperature	[K]
V_m	Volume of a solute particle	[m ³]
C	Concentration of MAI	[M]
C_0	Equilibrium concentration of MAI	[M]
σ_{sl}	Surface tension	[J m ⁻²]
G_c	Critical Gibbs free energy	[J]
V_{oc}	out-circuit voltage	[V]
J_{sc}	short-circuit current density	[mA cm ⁻²]
U_{offset}	Offset voltage for suppression charge extraction	[V]
U_{max}	Maximum voltage	[V]
j_0	Capacitive displacement current	[mA cm ⁻²]
A	Voltage increase rate	[V/s]
t_{max}	Time at maximum current	[s]
μ	Carrier mobility	[cm ² V ⁻¹ s ⁻¹]
r_A	Radius of A site cation	[nm]
r_X	Radius of X site anion	[nm]
r_{Pb}	Radius of Pb ²⁺	[nm]
t	Goldschmidt tolerance factor	

List of Figures

Figure 2.1 Schematic illustrations of fabrication process of perovskite solar cell using two-step spin-coated method.....	14
Figure 2.2 (a) Theoretical plot with Gibbs free energy versus crystal size in crystal growth process. Top and cross-sectional views of MAPbI ₃ crystal using FE-SEM and focused ion beam (FIB) SEM for the MAI solution concentration of (b) 0.038 M and (c) 0.063 M.	18
Figure 2.3 Plot of theoretically derived MAPbI ₃ grain size (Y) as a function of MAI concentration (X). The experimental data (filled square) were fit with a theoretical equation.	22
Figure 2.4 Top-view SEM images and cross-sectional FIB-SEM images for the MAPbI ₃ crystals grown at different temperature (MAI solution and substrate have the same temperature) of (a) and (b) -10 oC, (c) and (d) 20 oC and (e) and (f) 50 oC.....	24
Figure 2.5 (a) Short-circuit current density (J _{sc}), (b) open-circuit voltage (V _{oc}), (c) fill factor (FF) and (d) power Conversion Efficiency (PCE) of the perovskite solar cells with MAPbI ₃ crystals grown at different temperature.	27
Figure 2.6 ((a) UV-Vis absorption spectra of MAPbI ₃ perovskite films depending on reaction temperature. (b) External quantum efficiency (EQE) of perovskite solar cells employing MAPbI ₃ grown at different reaction temperature.	28
Figure 2.7 Photograph of MAPbI ₃ coated substrates depending on MAI	

concentrations and reaction temperature.	29
Figure 3.1 Schematic representation of fabrication procedure and plane-view scanning electron microscopy (SEM) images for the MAPbI ₃ perovskite layers obtained by direct one-step spin-coating of the DMF solution containing (a) MAI and PbI ₂ or (b) MAI, PbI ₂ and DMSO. (c) and (d) were prepared by same solution as (a) and (b), but diethyl ether was dripped while the film spinning.....	37
Figure 3.2 (a) Photos of MAPbI ₃ on FTO glass (a) before and (b) after annealing at 65 oC for 1 min and 100 oC 2 min. Fourier transform infrared spectrometer (FTIR) of (c) DMSO (solution), PbI ₂ •DMSO (powder), MAI•PbI ₂ •DMSO (powder) and (d) expanded the finger print region for the S=O vibrations.	41
Figure 3.3 X-ray diffraction patterns of perovskite films on FTO glass fabricated by using PbI ₂ :MAI:DMSO (1:1:1 mol%, red) and PbI ₂ :MAI:DMSO (1:1:2 mol%, black) solutions with diethyl ether treatment. Although both films were not annealed, these were crystallized spontaneously due to volatile DMSO. XRD peaks corresponding to PbI ₂ appeared in the case of PbI ₂ :MAI:DMSO (1:1:2) contrary to the case of PbI ₂ :MAI:DMSO (1:1:1). The XRD pattern (blue) represents perovskite film obtained after heat treatment.	42
Figure 3.4. UV-visible absorption spectra depending on aging time of the perovskite film prepared by adduct method. The film was stored at ambient conditions (Relative humidity > 45%) without encapsulation and using desiccator.	44
Figure 3.5 (a) The photo-CELIV current transients of perovskite solar cell	

consist of FTO/bl-Al₂O₃/mp-TiO₂/MAPbI₃/Spiro-MeOTAD/Ag in case of DMF or DMSO/DMF used as solvents for MAPbI₃. (b) The current peaks (Δj) of photo-CELIV current transients normalized by their displacement current of capacitance(j_0), respectively. Curves were fitted by polynomial fitting to compare charge extraction behaviour of sample with or without DMSO..... 48

Figure 3.6 (a) Plan-view SEM image of CH₃NH₃PbI₃ and (b) FIB-assisted cross sectional SEM image of full cell structure of perovskite solar cell based on the adduct-induced MAPbI₃. The thickness of bl-TiO₂, mp-TiO₂, MAPbI₃, spiro-MeOTAD and Ag were 40, 200, 400, 200 and 180 nm, respectively. (c)-(f) Histograms of short-circuit current density (J_{sc}), open-circuit voltage (V_{oc}), fill factor (FF) and power conversion efficiency (PCE) of 41 cells, respectively. (g) J-V curve and (h) external quantum efficiency (EQE) spectrum together with EQE data-based integrated J_{sc} for the best performing perovskite solar cell. J-V data were collected at reverse scan under AM 1.5G one sun illumination (100 mW/cm²). The aperture mask area was 0.125 cm². The data were collected with the 16 h-aged cells because Ag electrode-based device showed normally poor fill factor right after fabrication.... 51

Figure 3.7 (a) J-V curves measured depending on scan direction and scan rate. Measurement from V_{oc} to J_{sc} is referred to reverse scan (blue) and visa versa is forward scan (red). (b) Stabilized photocurrent density (black) and power conversion efficiency (red) measured at maximum power voltage of 0.86V for 250 seconds..... 55

Figure 4.1 Dependence of the Goldschmidt tolerance factor on the MA

fraction (x) of MA_xFA_{1-x}PbI₃. Dashed zone means region for cubic structure ($0.9 < t < 1$)..... 66

Figure 4.2 X-ray diffraction patterns of five different mixed perovskite films coated on ITO glass (x=0.2 (black), 0.4 (red), 0.6 (blue), 0.8 (green), and 1 (pink)) (a) before and (b) after degradation under one sun illumination at 50 % relative humidity for 10 hours. (c) Magnified XRD patterns around the peaks originating from PbI₂ and non-perovskite δ-phase. (d) Magnified XRD patterns for x=0.2 and 0.4... 68

Figure 4.3 Dependence of the normalized PCEs of ITO/C60/Perovskite/Spiro-MeOTAD/Au device on (a) the MA⁺ fraction (x), and (b) the Br- fraction (3-y). 69

Figure 4.4 (a) Absorption spectra and pictures of the MAPbI₃ perovskite film (b) before and (c) after ageing for 2 days under dark conditions at 90% RH. MAPbI₃ perovskites were transformed into transparent hydrated states after 2 days. (d) Absorption spectra and pictures of the MA_{0.6}FA_{0.4}PbI_{2.9}Br_{0.1} perovskite film (e) before and (f) after ageing under the same condition. (g) Time evolution of absorption spectra and pictures of MAPbI₃ (h) before and (i) after degradation under light soaking at 20% RH. (j) Time evolution of absorption spectra and pictures of MA_{0.6}FA_{0.4}PbI_{2.9}Br_{0.1} (k) before and (l) after degradation under the same condition. 72

Figure 4.5 Photovoltaic performance characteristics. (a) *J-V* curves of the best-performing device measured at various sweep delay times. (b) Stabilized photocurrent density (black) and power conversion efficiency (blue) measured at a bias voltage of 0.91V for 140 seconds.

(c) External quantum efficiency (EQE) spectrum and the integrated J_{sc} estimated from the measured EQE. Histograms of (d) short-circuit current density (J_{sc}), (e) open-circuit voltage (V_{oc}), (f) fill factor (FF), and (g) power conversion efficiency (PCE) of 47 cells..... 74

Figure 5.1 Device performance and stability depending on different ETLs.

$J-V$ curves of (a) ITO/ C_{60} (35nm)/ $MA_{0.6}FA_{0.4}PbI_{2.9}Br_{0.1}$ (500nm)/Spiro-MeOTAD(250nm)/Au(50nm) and (b) FTO/ TiO_2 (40nm)/ $MA_{0.6}FA_{0.4}PbI_{2.9}Br_{0.1}$ (500nm)/Spiro-MeOTAD(250nm)/Au(50nm) measured in the reverse (black) and forward (red) scans with a 200 ms sweep delay. (c, d) Time evolution of the normalized PCE measured under one sun illumination in ambient conditions (relative humidity = 30%) of the (c) C_{60} and (d) TiO_2 based devices.. 84

Figure 5.2 Degradation patterns depending on different ETLs. (a, b) Time

evolution of the FIB-SEM cross-sectional images of the (a) C_{60} and (b) TiO_2 based devices aged for 72 h under light illumination in ambient conditions. Scale bars = 200 nm. 85

Figure 5.3 Degradation patterns of the C_{60} - (left) TiO_2 - (right) based

devices employing $MAPbI_3$ perovskite, which were aged under one sun illumination in ambient conditions. Scale bars = 200 nm. As was shown in Fig. 1 for our mixed perovskite, the cell employing $MAPbI_3$ also showed the same pattern of degradation: for TiO_2 -based cell, the degradation begins from the interface between $MAPbI_3$ and TiO_2 electron extraction layer, but for C_{60} -based cell, the degradation begins from the opposite side of interface between $MAPbI_3$ and Spiro-MeOTAD hole extraction layer..... 86

Figure 5.4 Time evolution of the FIB-SEM cross-sectional images of the C_{60} (left) and TiO_2 (right) based devices employing $MA_{0.6}FA_{0.4}PbI_{2.9}Br_{0.1}$ perovskites, which were aged for 48 h under UV filtered (Edmund Optics, 425nm High Performance UV Longpass Filter) light illumination in ambient conditions. Scale bars = 200 nm... 87

Figure 5.5 Experiments for trapped charge driven degradation. (a) Experimental setup of corona discharge for ion generation, bubbling system for humidification, and SUS chamber for ion deposition and blocking light. Absorption spectra of the perovskite film measured at an interval of 18 hours during deposition of (b) positive nitrogen ions and (c) negative hydrogen ions at 40% relative humidity..... 92

Figure 5.6 Absorption spectra of the perovskite film under (a) continuous positive nitrogen and (b) negative hydrogen ion deposition in moisture-free dark condition..... 93

Figure 5.7 XRD patterns of the perovskite film before (red) and after (black) aged at 90% relative humidity for 2 days.. 93

Figure 5.8 Comparison of the degradation rates of $MAPbI_3$ and $MA_{0.6}FA_{0.4}PbI_{2.9}Br_{0.1}$ perovskite films at 40% relative humidity with positive nitrogen ion deposition. Absorption spectra were measured at an interval of 3 hr... 94

Figure 5.9 The effect of non-contact high electric field on the degradation of the perovskite film at high relative humidity (90%) under dark condition. 94

Figure 5.10 SEM and KPFM measurements. (a-d) Schematic illustration of perovskite degradation processes (left), (e-h) top-view (middle) and (i-

l) cross-sectional (right) SEM images of perovskite layers (a,e,i) before, (b,f,j) after 6 hours, (c,g,k) 12 hours, and (d,h,l) 18 hours by ion deposition in humidified nitrogen. The color change from dark brown to yellow in (a,b,c,d) represents the gradual degradation process. Black lines and their widths in (a,b,c,d) represent grain boundaries and degradation extent, respectively. Scale bars = 200 nm. (m) Topography and (n) surface potential profile of $\text{MA}_{0.6}\text{FA}_{0.4}\text{PbI}_{2.9}\text{Br}_{0.1}$ film obtained from KPFM measurements after deposition of N_2 positive ions..... 98

Figure 5.11 The top-view SEM images of the fresh and degraded perovskite films. The degraded samples were aged for 9 hours under one sun light illumination (first row) and ion charge deposition (second row), respectively.. 99

Figure 5.12 XRD patterns of the $\text{MA}_{0.6}\text{FA}_{0.4}\text{PbI}_{2.9}\text{Br}_{0.1}$ and MAPbI_3 film before and after degradation by trapped charges in the presence of moisture.. 100

Figure 5.13 Topographies (first column) and surface charge density profiles (second column) of untreated (first row), Ion-treated (second row), and light-illuminated (third and fourth row) $\text{MA}_{0.6}\text{FA}_{0.4}\text{PbI}_{2.9}\text{Br}_{0.1}$ perovskite film. The images in the third and fourth row were obtained from light on and off during the measurement, respectively. The images in the third column show 3D plots of topographies colored based on the surface potential values. Both images of light illuminated cases show clear charge trapping along grain boundaries, but the charge trap is more contrasted when KPFM operation is under the light on..... 101

Figure 5.14 Absorption spectra of the perovskite film under one sun illumination in nitrogen. Light was illuminated in a moisture-free condition.....	102
Figure 5.15 Synergetic effect of oxygen on degradation. Time evolution of the absorption spectra of $MA_{0.6}FA_{0.4}PbI_{2.9}Br_{0.1}$ films (a) in humidified nitrogen and (b) in humidified air measured at an interval of 3 hours during deposition of positive nitrogen ions. In both cases, the relative humidity is 40%.....	106
Figure 5.16 Absorption spectra of the perovskite film in dry air after deposition of positive nitrogen ions..	107
Figure 5.17 X-ray diffraction (XRD) patterns of the fresh and degraded samples of $MAPbI_3$ and $MA_{0.6}FA_{0.4}PbI_{2.9}Br_{0.1}$. The graph shows the magnified XRD patterns around the peak originating from I_2 (*).	108

Chapter 1. Introduction

1.1. Research Background and Objectives

Solar cell technology have a long history from the first generation Si solar cell to currently-developed numerous types of solar cells adopting new materials. To date, the direction of the history flows to replace expensive Si solar cells. Many researchers cannot help concentrating on cheap materials functioning as a light harvester, which leads to exploration of organic materials. Organic materials-based photovoltaics were on the rise as next-generation solar cells, however, their relatively lower performance and stability drag their industrialization down. In the meantime, one of organic inorganic hybrid materials, $\text{CH}_3\text{NH}_3\text{PbI}_3$ (MAPbI_3)-based photovoltaics were reported for the first time in 2009 from a group of Prof. Miyasaka[1]. The device employed liquid electrolytes, which resulted in low stability due to chemical reaction between liquid electrolyte and MAPbI_3 perovskite. Four years after, Prof. Park reported the solid-state MAPbI_3 solar cells, demonstrating the best PCE of 9.7%[2], which was comparable to the best PCE of organic photovoltaics (OPV) or dye-sensitized solar cells (DSSC) at that time. These organic inorganic hybrid perovskite materials have not only

advantages of organic materials such as low cost and low-temperature processability but also excellent properties as a light harvesting material such as high extinction coefficient, direct band gap and long carrier diffusion length[1-4]. After that, the perovskite solar cells quickly renewed the world-best PCE record as a consequence of worldwide interest from a lot of solar cell researchers[5-7].

Unlike general organic materials, these organic inorganic hybrid perovskites are crystalline materials which can be formed by crystallization process[8]. Perovskite thin layers in photovoltaic devices are usually the set of few hundreds nanometer-sized crystals because the thickness of the layers is about 500 nm. Since the quality of the perovskite thin layer is directly associated with photovoltaic performance of perovskite photovoltaics, it is essential to improve both the quality of each crystals and overall morphology of films[9]. Charge generation and collection will be improved when the crystal size is bigger and the defects of the crystals is less[10]. The morphology is also crucial in charge separation and transport. The more dense and homogeneous the film is, the better performance can be realized. Accordingly, at the initial stage of perovskite photovoltaic research, there were a lot of study on the formation of MAPbI_3 films to improve the PCE. Until sequential deposition

method, so-called two-step method, was reported by a group of Prof. Gratzel[3], MAPbI₃ films were formed by spin-coating precursor solution dissolving PbI₂ and CH₃NH₃I (MAI) in GBL[1,2,8]. Since the solubilities of PbI₂ and MAI to polar aprotic solvent like GBL and DMF are quite different, PbI₂ is crystallized faster than MAI during spin-coating process which is attributed to poor film morphology. To improve the film quality, Gratzel et al. introduced the two-step method, in which MAI solution in 2-propanol reacted with the solid PbI₂ film after the PbI₂ film was formed by spin-coating solution dissolving PbI₂ in DMF first. They achieved the best PCE of 15% via this method, leading to dramatic performance increase of perovskite solar cells. After that, Im et al. reported the 17% PCE via modified two-step method[10], in which the concentration of MAI was optimized to obtain MAI perovskite films with large grain size. In the paper, MAPbI₃ cuboid size is determined by the concentration of MAI, however, the reason was elusive. It was required to understand the crystallization mechanism and what determines the cuboid size and the film quality. In chapter 2, the crystallization process is analyzed based on thermodynamics of chemical reaction in two-step method[11]. By tracking change in Gibbs free energy during the crystallization, critical energy for spontaneous crystal growth can be obtained. From the critical energy,

the number of nuclei to be spontaneously crystallized is calculated with assuming boltzmann distribution of reactants. Finally, the grain size equation for this two-step method is derived as a function of concentration, temperature and surface tension. The trend of grain size depending on concentration is well fitted with experimental results of the previous work[10]. the reaction temperature considerably affect the cuboid size of perovskite films as known from the equation, the effect of which was experimentally confirmed. The cuboid size increases as temperature increases, which finally leads to high short-circuit current. However, overall photovoltaic performance decreases due to low open-circuit voltage as a consequence of low surface coverage because of three dimensional crystal growth. The study can provide which parameters determine crystal size and photovoltaic performance as a fundamental analysis.

Meanwhile, researchers tried to wash out solvent rapidly during spin-coating by dripping nonpolar solvent as new methods [12,13]. When perovskite precursor solution dissolving both PbI_2 and MAI in polar aprotic solvent was spin-coated on the substrate, polar aprotic solvent could be selectively washed out by dripping nonpolar solvent and PbI_2 and MAI could be simultaneously solidified. The different solubility of PbI_2 and MAI can be overcome via such nonpolar solvent dripping approach. However, since perovskites are

immediately crystallized at the moment of nonpolar solvent dripping, it is difficult to control the crystallization process[13]. Additionally, perovskite crystals are formed with small grain size as a consequence of fast crystallization. Various nonpolar solvent for dripping and polar aprotic solvent for dissolving both lead halide and organic halide are examined through experiments. A group of Prof. Seok reported solvent engineering method, in which precursor solution prepared by dissolving lead halide and organic halide in GBL and DMSO (7:3) mixed solvent was spin-coated with toluene dripping[12]. The intermediate MAI-PbI₂-DMSO phase was formed right after spin-coating, which finally changed into dark brown perovskite films by heating. It is well known that DMSO have interaction with lead halide as can be seen in the previous reports [14,15]. DMSO could be used to retard crystallization of lead iodide by adduct formation. To get high performance and reproducibility under such one-step methods with dripping treatment, deliberate fabrication process had been still necessary. Sulfur atom of DMSO molecule can readily provide unshared electron pair to lead atom of lead iodide, which results in lewis base adduct formation[16]. The adduct state can be maintained when equimolar DMSO exists. To control the molar amount of DMSO after spin-coating, nonpolar solvent should be carefully chosen. The widely used nonpolar

solvents for dripping, as mentioned above, were toluene and chlorobenzene, but such solvents are miscible with DMSO. In this regard, the amount of DMSO would be different depending on spin-coating and dripping condition. In chapter 3, lewis base adduct method for highly reproducible and efficient perovskite films was introduced, in which diethyl ether is employed as a nonpolar dripping solvent to selectively wash out DMF solvents[16]. The precursor is prepared by dissolving PbI_2 , MAI, and equimolar DMSO in DMF. The adduct was characterized by FT-IR measurements to define the adduct film. Perovskite photovoltaics fabricated via adduct method show improved charge mobility and extraction through photo-CELIV measurement, and their photovoltaic performance is verified from J-V curves of 41 cells, presenting the best PCE of 19.7% and averaged PCE of 18.3 with small standard deviation.

Although MAPbI_3 films can be well-defined via adduct method, the stability against light and air was still not guaranteed[17]. After the decomposition of perovskite materials into lead iodide, the device can generate electrical energy from solar light no more. Therefore, to delay the decomposition must be the highest priority for practical uses of perovskite photovoltaics. MAPbI_3 -based perovskite devices have shown fast deterioration under light illumination[17], which is indicative of low possibility of commercialization itself. But, it is

possible not only to engineer chemical compositions of these perovskite materials but also to modify structural phase by addition of different organic cation such as formamidinium($\text{HC}(\text{NH}_2)_2$, FA) and halide anion (Cl, Br)[5]. In other words, the resistance against light and air can be enhanced via such compositional engineering approach. To stabilize the crystal structure of perovskite materials, the Goldschmidt tolerance factor (t), which is calculated from the ratio of the ionic radii, should be adjusted in the range from 0.9 to 1 corresponding to undistorted cubic phase[18]. In the case of MAPbI_3 perovskite, the t value is 0.84 due to small organic cation and big halide anion[19], which cause the distortion of crystal structures. As the ionic radius of FA cation is bigger than that of MA cation, the t value can be tuned to be close to 1 by incorporation of FA cation. In chapter 3, new compositional perovskites that is more efficient and stable than conventional MAPbI_3 are developed in the mixed cation and/or halide anion system of $\text{MA}_x\text{FA}_{1-x}\text{PbI}_y\text{Br}_{3-y}$. [20] $\text{MA}_{0.6}\text{FA}_{0.4}\text{PbI}_{2.9}\text{Br}_{0.1}$ perovskites show not only the enhanced stability under one sun illumination in ambient air condition, but also those-base photovoltaic devices demonstrate the best PCE of 20.2 % without J-V curve hysteresis. It is notable that new mixed perovskite is not changed into hydrated state under high humidity (90%). On the contrast, MAPbI_3 film is hydrated under the same condition rapidly.

Such improvement is mainly attributed to structurally stable perovskite composition via tuning the t value.

While the perovskite materials itself have been optimized for the stability and performance, the stability of perovskite-based photovoltaic devices have been still troubled and the reason why the performance of perovskite solar cells have shown fast decay under light illumination is still elusive[21]. The lifetime of the device are highly dependent on the kind of charge selective layers regardless of external encapsulation[22]. Namely, different charge selective layers determine charge carrier extraction and transport, which would be the reason why the device stability is influenced by charge selective layers. Such characteristics would be associated with different J-V curve hysteresis depending on charge selective layers[20,23]. In this respect, the effect of charge on the stability of perovskite materials and those-based devices should be investigated to overcome short device lifespan under light illuminated condition. It is critical to verify degradation mechanism of perovskite solar cells.

In chapter 5, by analyzing the degradation pattern of perovskite solar cells depending on different electron transport layers, it is hypothesized that charges trapped along interfaces would be responsible for irreversible degradation[20]. To prove this, a novel experimental setup using corona discharger is used to deposit charges

on the perovskite surface and change in perovskite films was observed with or without water molecules. The degradation occurred only when both charges and water molecules simultaneously exist, which indicates that water-induced degradation of perovskite takes place in the presence of trapped charges. The degradation begins at grain boundaries of perovskite surface. Irreversible degradation is attributed to charges trapped along grain boundaries. Finally, the degradation scenario is suggested from these observations in addition to the synergetic effect of oxygen on degradation.

1.2. Thesis Outline

This thesis consists of six chapters. This Chapter 1 is devoted to overall introduction of this thesis. Next four chapters deal with experiments, results and discussions about my thesis entitled “Study on Formation and Decomposition of Perovskite Crystal for Highly Efficient and Long-term Stable Perovskite Solar Cells”

Chapter 2 focuses on perovskite crystal growth based on thermodynamics and Chapter 3 proposes lewis base adduct method to fabricate perovskite films. These two chapters suggests fabrication principles and methods for perovskite solar cells with high performance.

Chapter 4 is dedicated to a new mixed perovskite material in the mixed cation and/or halide system of $MA_xFA_{1-x}PbI_yBr_{3-y}$, which shows both improved performance and long-term stability. Lastly, chapter 5 deals with fundamental mechanism of degradation of perovskite solar cells.

Chapter 2.

Thermodynamic Regulation of Perovskite ($\text{CH}_3\text{NH}_3\text{PbI}_3$) Crystal Growth

Published in *Journal of Materials Chemistry A*, 2015, 3, 19901

2.1. Introduction

Research on solid-state perovskite solar cells based on the light harvester, methylammonium lead iodide, MAPbI_3 ($\text{MA} = \text{CH}_3\text{NH}_3$), has received considerable attention due to their low-cost technology, ease of processing and excellent photovoltaic performances. Following the first report on a 9.7% efficient perovskite solar cell in 2012,[2] the power conversion efficiency (PCE) of the device has been developed during a number of studies[1,4]. As a result, a PCE of 20.1% was reported in 2014[6], which is the highest certified value among organometal halide perovskite solar cells. Solution-processed techniques using onestep[12,13]/two-step[3,10] and vapor deposition methods[4] have been proposed to improve the potential performance of the perovskite solar cells. In particular, a two-step solution process, which involves sequential deposition of PbI_2 and MAI reacting readily to form MAPbI_3 , has been used due to the

possibility of controlling the fabricated grain sizes[4,24]. It is important to note that the grain sizes of the perovskite active layer affect the photovoltaic performances.[25,26] It was reported that MAPbI₃ grain sizes could be controlled by changing the MAI concentration, which led to enhancement of the properties of the solar cell device.[10] However, there are many other factors, such as temperature, surface tension and humidity, that affect the performances of perovskite solar cells by engineering the MAPbI₃ grain sizes.[25,27,28]

Herein, we report a fundamental analysis using a thermodynamic equation and temperature-controlled two-step solution engineering, which was used to investigate the correlation of the MAPbI₃ grain sizes with reaction temperature. Deriving a thermodynamic reaction model equation from Gibbs free energy, we demonstrate that the grain sizes of the MAPbI₃ active layer can be controlled not only by the MAI concentration but also by the reaction temperature of a two-step process that involves spin-coating MAI on the PbI₂ film. It is found that the temperature in the two-step coating process is crucial in determining the MAPbI₃ grain sizes and the performance of fabricated solar cells.

2.2. Results and discussion

The fabrication process of MAPbI₃ perovskite solar cell using two-step spin coating method is schematically illustrated in Figure 2.1. To form the PbI₂ crystallized film, 1 M N,N-dimethylformamide (DMF) solution of PbI₂ is spin-coated on the mp-TiO₂/bl-TiO₂/FTO substrate, where mp and bl stand for mesoporous and blocking, and annealed on a hot plate as shown in Figure 1a. Subsequently, MAI solution in 2-propanol is spread on PbI₂ film in order to crystallize MAPbI₃ perovskite (Figure 1b).[29]

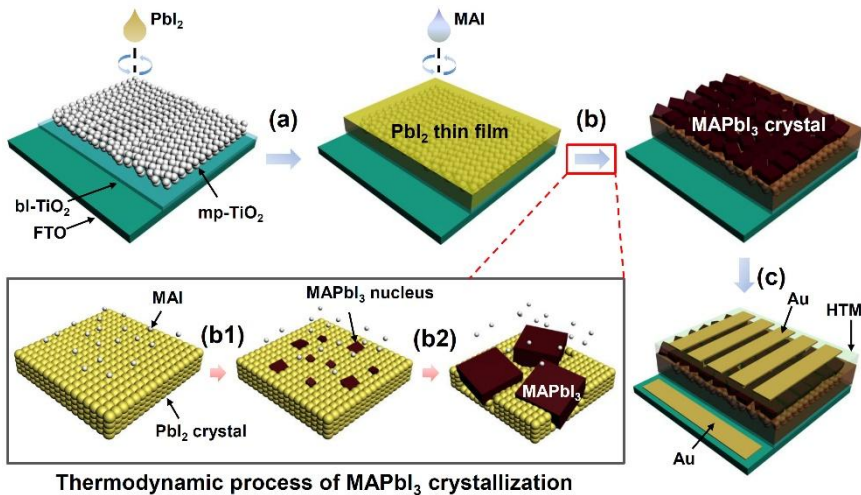
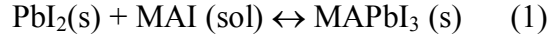


Figure 2.1 Schematic illustrations of fabrication process of perovskite solar cell using two-step spin-coated method. (a) First, PbI₂ solution (1 M in DMF) was spin-coated on the mesoporous (mp)-TiO₂ layer deposited on fluorine-doped tin oxide (FTO) substrate with the thin blocking (bl)-TiO₂ film, followed by annealing to form the PbI₂ film. (b) Second, MAI solution (0.05 M in 2-propanol) was loaded on the PbI₂ film in order to crystallize MAPbI₃ perovskite and then spun after 30 sec. (b1) MAPbI₃ nuclei were formed while MAI solutes constantly collide with PbI₂ film. (b2) MAPbI₃ nuclei selectively grew up based on statistical thermodynamic model. (c) Spiro-MeOTAD was spin-coated on the MAPbI₃ film and Au electrode was thermally evaporated to complete solar cell.

The chemical reaction to form MAPbI₃ in two-step procedure can be expressed as equation 1,



where MAI concentration in 2-propanol is determinant for the direction of the chemical reaction. Higher MAI concentration will push the reaction to right due to shift of equilibrium, leading to crystallization of perovskite. In the detailed process of forming perovskite, MAI constantly collides with solid PbI₂, which leads to form MAPbI₃ nuclei by probabilistic model. Then the tiny-sized nuclei which have enough energy for crystallization can selectively grow bigger according to thermodynamic model. The change of Gibbs free energy per unit volume (ΔG_V) with thermodynamic mechanism of crystallization is calculated by equation 2,[30]

$$\Delta G_V = - \frac{kT}{V_m} \ln \frac{C}{C_0(T)} \quad (2)$$

where k is the Boltzmann constant, T is the temperature of reaction, C is the concentration of MAI, C_0 is the equilibrium concentration of MAI, and V_m is the volume of a solute particle. The C_0 depends on temperature. When the crystallization occurs in solution phase, the change of Gibbs free energy by surface tension between the surface of crystal and solution (ΔG_S) should be considered together, and it can be written as equation 3,

$$\Delta G_s = \overline{\sigma_{sl}} \quad (3)$$

where $\overline{\sigma_{sl}}$ is the average surface tension. Since MAPbI₃ perovskite is a tetragonal structure at room temperature, the shape of MAPbI₃ can be assumed to be cube. Total change of Gibbs free energy (ΔG) for the two-step solution process is thus expressed as equation 4, [31]

$$\Delta G = -a^3 \frac{kT}{V_m} \ln \frac{C}{C_0(T)} + 6a^2 \overline{\sigma_{sl}} \quad (4)$$

where a is the length of cubic edge, a^3 is the volume of cube, and $6a^2$ is the total surface area of cube. By differentiating equation 4 with respect to a , a critical point where ΔG is maximized can be calculated by solving equation 5.

$$\frac{d\Delta G}{da} = -3a^2 \frac{kT}{V_m} \ln \frac{C}{C_0(T)} + 12a \overline{\sigma_{sl}} = 0 \quad (5)$$

As a result of equation 5, the critical size (a_c) and the critical Gibbs free energy (ΔG_c) are expressed as equation 6 and equation 7.

$$a_c = \frac{4\overline{\sigma_{sl}}}{\frac{kT}{V_m} \ln \frac{C}{C_0(T)}} \quad (6)$$

$$\Delta G_c = \frac{32\overline{\sigma_{sl}}^2}{\left(\frac{kT}{V_m} \ln \frac{C}{C_0(T)}\right)^2} \quad (7)$$

The change of Gibbs free energy is presented as a function of the size of perovskite crystal in **Figure 2.2**, where it is noted that Gibbs free energy is affected dominantly by surface tension. Gibbs free energy increases when size is smaller than the critical size, whereas decrease in Gibbs free energy is more dominant when size is bigger than the critical size. Consequently, perovskite nuclei which have sufficient energy over the critical energy are expected to be grown by spontaneous chemical reaction. As a result, the perovskite crystal would grow up until all PbI_2 turn into perovskite. Therefore, the average grain size of MAPbI_3 is controlled by two concepts: 1. the crystal growth of perovskite is determined by the critical energy (G_c) and 2. each nucleus will spontaneously grow up until it contacts with surrounding crystals at grain boundaries. Since energy distributions of reactants follow a Boltzmann distribution based on statistical thermodynamics, the number of nuclei which has potential to become the crystal is proportional to $e^{\frac{-\Delta G_c}{kT}}$.²⁴ The average volume of perovskite crystal is inversely proportional to the number of nuclei (n)

per unit volume because increase in number of nuclei inhibits crystal growth due to the decreased space for crystal growth. Therefore, the grain size (Y) has the following relation.

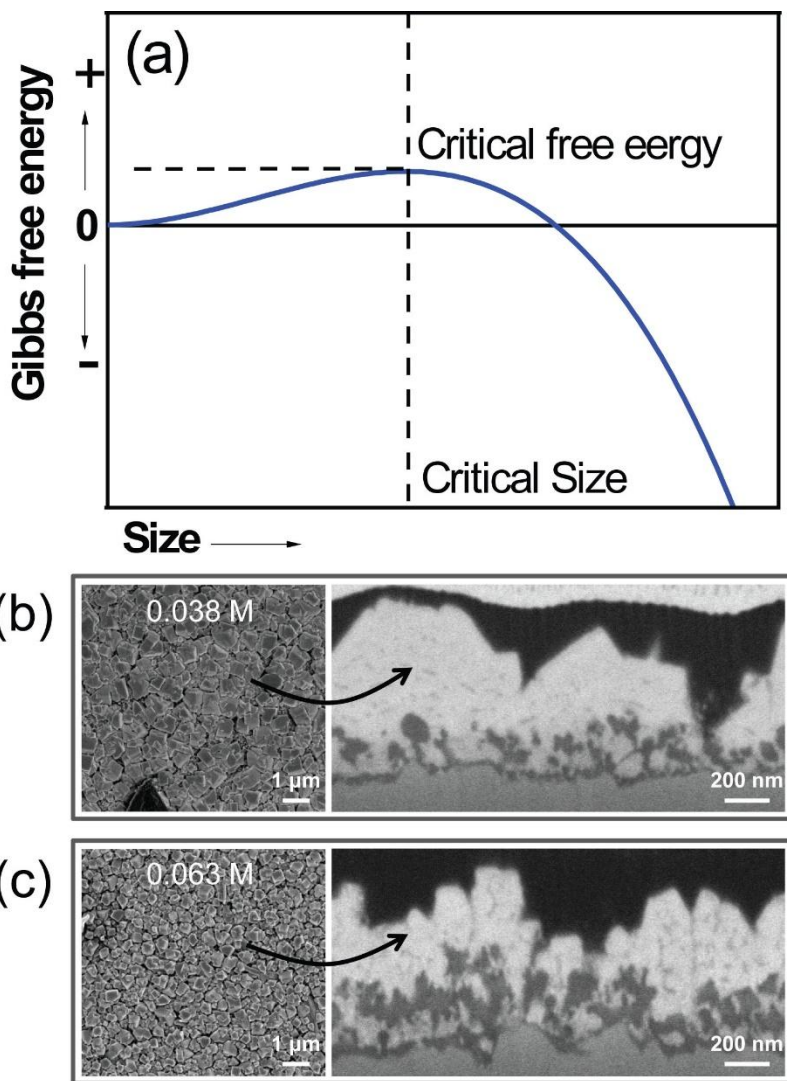


Figure 2.2 (a) Theoretical plot with Gibbs free energy versus crystal size in crystal growth process. Top and cross-sectional views of MAPbI₃ crystal using FE-SEM and focused ion beam (FIB) SEM for the MAI solution concentration of (b) 0.038 M and (c) 0.063 M.

$$Y(\text{grain size}) \propto a \propto \sqrt[3]{\frac{1}{n}} \propto e^{\frac{\Delta G_c}{3kT}} \quad (8)$$

From the equation 7 and the relation (8), we can derive the interaction formula between grain sizes and MAI concentration in equation 9

$$\ln Y = \frac{32\sigma_{sl}^3}{3kT\left(\frac{kT}{V_m}(\ln X - \ln C_0(T))\right)^2} + C' \quad (9)$$

where X is the MAI concentration and C' is constant. It is demonstrated that the equation 9 correctly predicts grain sizes depending on MAI concentrations which were measured previously elsewhere,[10] as shown in **Figure 2.3**.

Derive equation of thermodynamic MAPbI₃ reaction process.

From the relation (8), we could derive a logarithmic formula by introducing constant C'.

$$\ln Y(\text{grain size}) = \frac{\Delta G_c}{3kT} + C' \quad (10)$$

Substituting equation (7), we could derive a formula about relationship between grain size and concentration.

$$\ln Y = \frac{1}{3kT} \frac{32}{\left(\frac{kT}{V_M} \ln \frac{c}{c_0}\right)^2} + C' \quad (11)$$

Finally, the equation could be obtained by replacing concentration with X.

$$\ln Y = \frac{32\sigma_{sl}^3}{3kT\left(\frac{kT}{v_m}(\ln X - \ln C_0(T))\right)^2} + C' \quad (12)$$

Here, the equation was summarized as a simple formula with substitution other terms to constant, except for concentration.

$$\ln Y = \frac{B}{(\ln X - A)^2} + C$$

It would be assumed that the equilibrium concentration is 0.02 M of MAI solution at room temperature since the PbI_2 film could not react with 0.02 M of MAI solution. In this manner, a value of A would be -3.19, which means natural log value of equilibrium constant. The other value of B and C were mathematically evaluated in order that the model was fitted with an actual data in **Table 2.1**, as result, B and C were 1.22 and 3.73 respectively (see **Figure 2.3**).

Table 2.1. Grain sizes, short-circuit photocurrent density (J_{sc}), open-circuit voltage (V_{oc}), fill factor (FF) and power conversion efficiency (PCE) versus MAPbI₃ concentration. Data were taken from reference S1.

MAI Concentration	0.038 M	0.044 M	0.050 M	0.057 M	0.063 M
Grain Size (nm)	720	360	190	130	90
J_{sc} (mA/cm ²)	21.68	-	21.01	-	19.27
V_{oc} (V)	1.065	-	1.090	-	1.080
FF	0.709	-	0.711	-	0.646
PCE (%)	16.36	-	16.27	-	13.45

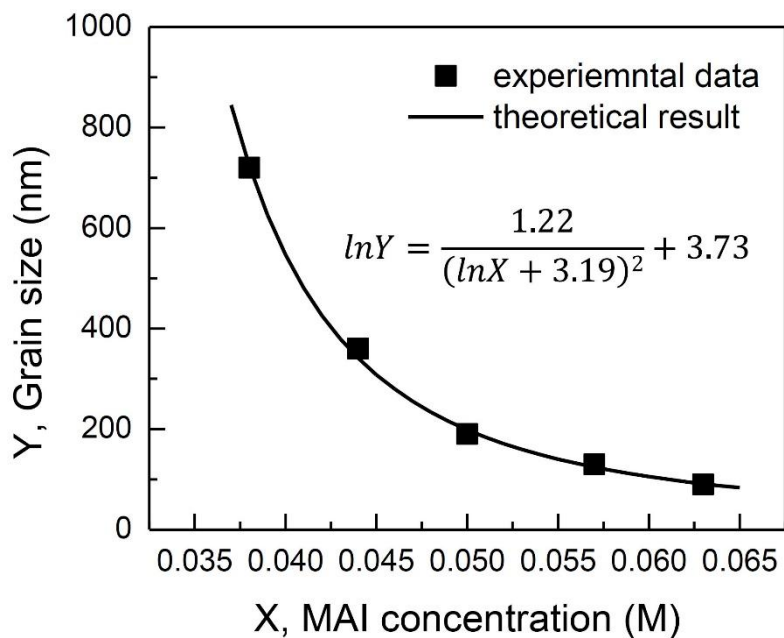


Figure 2.3 Plot of theoretically derived MAPbI₃ grain size (Y) as a function of MAI concentration (X). The experimental data (filled square) were fit with a theoretical equation.

According to equation 9, MAPbI₃ crystal size is controlled not only by the concentration of MAI but also by temperature. To see the temperature effect, both the substrate and the MAI solution are pre-heated at different temperature of -10 °C, 20 °C and 50 °C, in which the MAI concentration is fixed to 0.050 M. As shown in the SEM images in **Figure 2.4a-f**, the grain size increases as temperature increases. As the temperature of MAI solution increases, the equilibrium concentration of the chemical reaction also increases due to the high solubility of MAI. Therefore, the critical free energy at high temperature is bigger than that at low temperature from the equation 7, which determines the number of nuclei based on the relation (8). As a result, the number of nuclei growing up MAPbI₃ crystal is decreased, which leads to increase the MAPbI₃ grain sizes. Top-view SEM images (**Figure 2.4a,c,e**) and cross-sectional FIB-SEM images (**Figure 2.4b,d,f**) clearly show that the MAPbI₃ grain size changes with temperature, which can be explained by our theoretical analysis using the eq 9. It is noted that MAPbI₃ grown at 50 °C shows large gaps between crystals, which causes direct contact between mp-TiO₂ and spiro-MeOTAD.

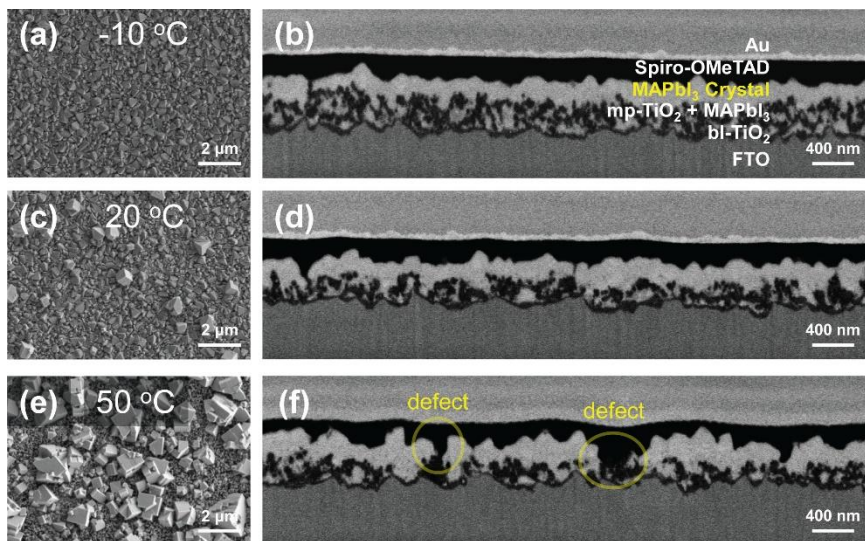


Figure 2.4 Top-view SEM images and cross-sectional FIB-SEM images for the MAPbI₃ crystals grown at different temperature (MAI solution and substrate have the same temperature) of (a) and (b) -10 °C, (c) and (d) 20 °C and (e) and (f) 50 °C.

Effect of reaction temperature on photovoltaic parameters is investigated. **Figure 2.5** shows the measurement results depending on reaction temperature with short-circuit current density (J_{sc}), open-circuit voltage (V_{oc}), fill factor (FF) and power conversion efficiency (PCE). As can be seen in **Figure 2.5a**, the J_{sc} is improved as reaction temperature increases, which may be due to increase in light absorption by increase in grain size (see **Figure 2.6**). It is noted that the corresponding perovskite colors become darker with increasing grain size. On the other hand, the significantly lowered V_{oc} and FF are observed for 50 °C (**Figure 2.5b**), which is probably related to the defects in perovskite layer as shown in **Figure 2.4f**. The defects caused by increasing grain size provide recombination sites between mp-TiO₂ and spiro-MeOTAD. V_{oc} and FF will be dependant on the thickness of mp-TiO₂ layer and whole perovskite layer. These are slightly improved for 20 °C compared to -10 °C because of higher density and compressed mp-TiO₂ layer (~ 250 nm) and whole perovskite layer (~450 nm), which is thinner than those of -10 °C (~400 nm and ~600 nm, respectively), as shown in **Figure 2.4d**. It is supposed that the compressed mesoporous TiO₂ layer results from volume expansion of MAPbI₃ capped on mesoporous TiO₂ layer by increasing MAI solution temperature. As a results, the PCE is highest for the reaction temperature of 20 °C. Photovoltaic parameters for the best performing devices are represented in **Table 2.2**.

Reaction Temperature	J_{sc} (mA/cm ²)	V_{oc} (V)	FF	PCE (%)
- 10 °C	19.33	1.010	0.70	13.67
20 °C	19.84	1.014	0.71	14.28
50 °C	20.29	0.956	0.69	13.38

Table 2.2. Short-circuit photocurrent density (J_{sc}), open-circuit voltage (V_{oc}), fill factor (FF) and power conversion efficiency (PCE) depending on reaction temperature. The data represent the best performing device for each reaction temperature.

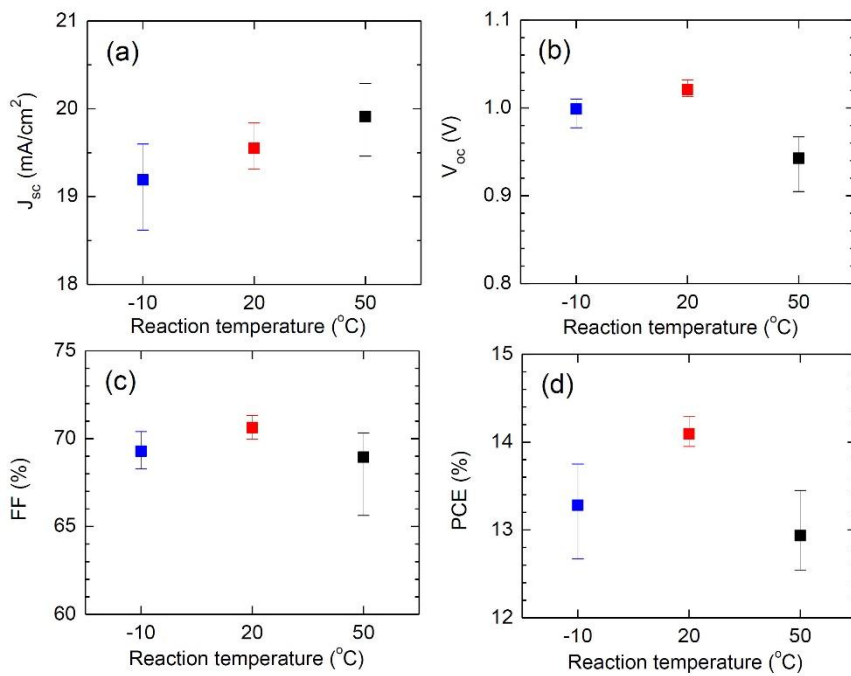


Figure 2.5 (a) Short-circuit current density (J_{sc}), (b) open-circuit voltage (V_{oc}), (c) fill factor (FF) and (d) power Conversion Efficiency (PCE) of the perovskite solar cells with $MAPbI_3$ crystals grown at different temperature.

Figure 2.6a shows that the absorbance is higher for 20 °C and 50 °C than for -10 °C. Decrease in absorbance with decreasing grain size was observed in the previous work,[10] which is in part related to the higher reflectance. Relatively low absorbance of MAPbI₃ grown at -10 °C results from smaller grain size. Large crystals with gaps between crystals have beneficial to external quantum efficiency (EQE) especially at long wavelength (**Figure 2.6b**) due to enhanced internal light scattering, which is responsible for higher J_{sc} from 50 °C.

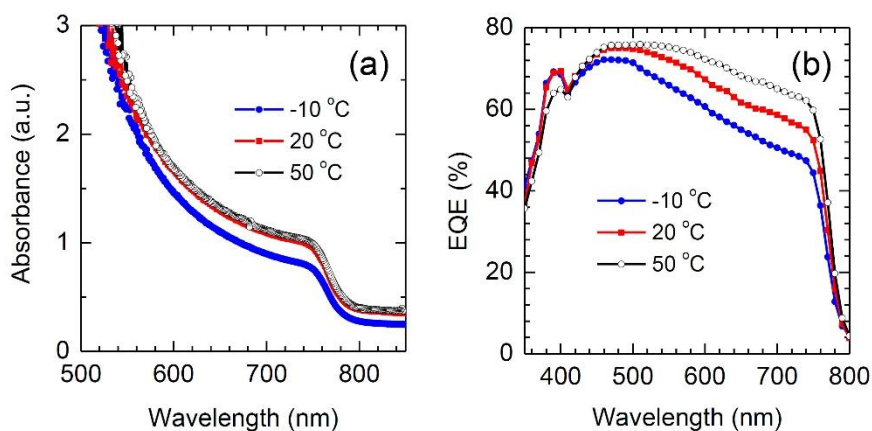


Figure 2.6 (a) UV-Vis absorption spectra of MAPbI₃ perovskite films depending on reaction temperature. (b) External quantum efficiency (EQE) of perovskite solar cells employing MAPbI₃ grown at different reaction temperature.

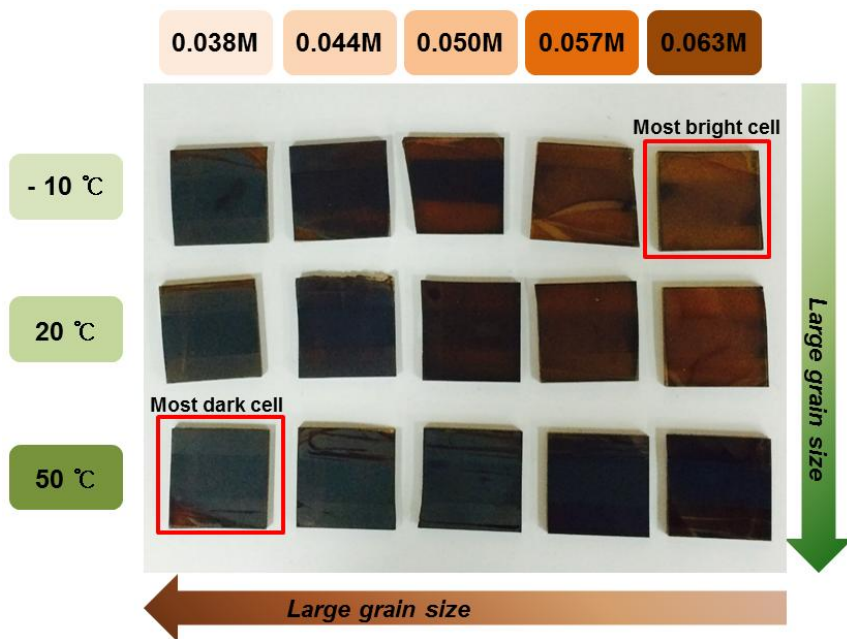


Figure 2.7 Photograph of MAPbI₃ coated substrates depending on MAI concentrations and reaction temperature.

2.3. Conclusions

We have presented a theoretical approach using thermodynamic analysis derived from Gibbs free energy to explain the crystal growth of MAPbI₃ and found that grain size of MAPbI₃ crystal were clearly dependent on reaction temperature. The grain size was increased with reaction temperature, which could be explained by the thermodynamic model. Photovoltaic performance was significantly altered by reaction temperature, which was mainly due to the MAPbI₃ grain size and morphology of the resultant MAPbI₃ film. MAPbI₃ grown at 20 °C showed better performance compared to lower or higher reaction temperature.

2.4. Experimental methods

Materials synthesis: Mesoporous 50-nm sized TiO₂ nanoparticles were hydrothermally synthesized using 20-nm sized seed particles as described elsewhere.²⁵ 1.4 g of the TiO₂ paste, which consists of nanocrystalline TiO₂, terpineol, ethylcellulose and lauric acid with a nominal ratio of 1.25 : 6 : 0.9 : 0.3 in wt%, was diluted in 10 ml ethanol to prepare mesoporous TiO₂ film. MAI was synthesized by reacting 27.8 ml of CH₃NH₂ (40 wt% in methanol, TCI) with 30 ml of HI (57 wt% in water, Aldrich) in a round bottom flask in ice bath for 2 h.[32] Using a rotary evaporator, the resulting MAI was collected at 50 °C for 1h, which was washed with diethyl ether and dried in vacuum chamber for 12 h.

Fabrication of Perovskite Solar Cells: Fluorine-doped tin oxide-coated (FTO) glass substrate (Pilkington, TEC-8, 8Ω/sq) was cleaned using UV/Ozone treatment for 15 min and sonicated in ethanol after washing with detergent liquid, acetone and DI water. A thin compact TiO₂ blocking (bl) layer was deposited on FTO by spin-coating 0.15 M titanium diisopropoxide di(acetylacetonate) (Sigma-Aldrich, 75 wt% in isopropanol) in 1-butanol (Sigma-Aldrich, 99.8%) at sequentially increasing spin rate of 700 rpm for 8 s, 1000 rpm for 10 s and 2000 rpm for 40 s. The bl-TiO₂ layer was heated at 125 °C for 5 min. A mesoporous (mp) TiO₂ layer was formed on the bl-TiO₂

layer by spin-coating the diluted TiO₂ paste solution at 2000 rpm for 20 s and annealing at 550 °C for 1 h. After UV/Ozone treatment for 30 min, the substrate was treated with 20 mM aqueous TiCl₄ (Sigma-Aldrich, > 98 %) by immersing the mp-TiO₂ coated substrate at 90 °C for 10 min, which was followed by annealing again at 500 °C for 30 min. The deposition of MAPbI₃ perovskite active layer on the mp-TiO₂ layer was conducted by two-step process. First, 30 µl of PbI₂ solution (1 M (1.844 g) of PbI₂ (Sigma-Aldrich, 99 %) dissolved in 4 ml of *N,N*-dimethylformamide (DMF, Sigma-Aldrich, 99.8%)) was spin-coated on the mp-TiO₂ coated substrate at 6000 rpm for 20 s, which was dried at 40 °C for 3 min and 100 °C for 5 min sequentially. Second, 200 µl of 0.05 M (8 mg/ml) MAI in 2-propanol (Sigma-Aldrich, 99.5%) was spin-coated on the PbI₂ film at 3000 rpm for 20 s in 30 s of loading time for MAPbI₃ crystallization and dried at 100 °C for 5 min. Prior to the MAI coating process, the three MAI solutions with different temperature of -10 °C (in a dry ice chamber), 20 °C (room temperature) and 50 °C (using pre-heated hot plate) were prepared. The hole transport material (HTM) was deposited on the substrate by spin-coating a 72.3 mg of spiro-MeOTAD solution in 1 ml Chlorobenzene, to which 28.8 µl of 4-*tert*-butyl pyridine and 17.5 µl of lithium bis(trifluoromethanesulfonyl)imide (Li-TFSI) solution (520 mg Li-TFSI in 1

ml acetonitrile (Sigma–Aldrich, 99.8 %) at 4000 rpm for 20 s. Finally, gold (Au) was thermally evaporated on the top of the HTM for the counter electrode under $\sim 10^{-6}$ Torr vacuum condition at $\sim 1 \text{ \AA/s}$.

Characterization: The morphologies of the MAPbI_3 layer and the fabricated perovskite solar cells were examined by using a high-resolution scanning electron microscope (HR SEM, JSM-7600F, JEOL) and a focused ion beam assisted SEM (FIB-SEM, Auriga, Carl Zeiss). To avoid charging effect, a 10 nm-thick Pt layer was deposited on the top of substrate. The absorbance of MAPbI_3 perovskite active layer was analyzed by using UV/Vis spectrometer (Lambda 45, PerkinElmer) in the range of wavelength from 500 to 900 nm. Photocurrent density–voltage curves were recorded using a solar simulator (Oriel Sol 3A class AAA) equipped with a 450 W Xenon lamp (Newport 6279NS) and a Keithley 2400 source meter under AM 1.5G one sun illumination (100 mW/cm^2). Aperture mask was used while measuring the devices at reverse scan mode at 200 ms scan rate. External quantum efficiency (EQE) was measured using a specially designed EQE system (PV measurement Inc.), where a 75 W Xenon lamp (USHIO, Japan) was used as a source light to generate monochromatic beam.

Chapter 3.

Lewis-base Adduct Assisted Perovskite Crystal Growth for High Performance

Published in *Journal of American Chemical Society*, 2015, 137 (27), 8696-8699

3.1. Introduction

Since the report on the 9.7% solid-state perovskite solar cell employing MAPbI₃ (MA = CH₃NH₃) and spiro-MeOTAD in 2012,[2] overcoming the dissolution problem of MAPbI₃ in liquid electrolyte observed in the two important pioneer works in 2009 and 2011,[1,8] there is a surge in perovskite solar cell researches due to facile fabrication procedure and superb photovoltaic performance in both mesoscopic structure and planar structure.[4-6,26,33] As a result, a power conversion efficiency (PCE) of 20.1% was certified by national renewable energy laboratory.[6]

MAPbI₃ layer for perovskite solar cell can be prepared using either one-step coating,[1,8] or sequential two-step coating.[3,10] It was reported that photovoltaic performance of devices prepared by two-step coating was superior to one-step method.[9] Recently solvent engineering method was proposed in one-step spin

coating,[12] where DMSO was used as a co-solvent in the gamma-butyrolactone (GBL) solution containing MAI and PbI_2 . One-step coated film was washed with toluene while spinning to get rid of solvent and to form a so-called intermediate phase of MAI- PbI_2 -DMSO, by which an average PCE of about 15% together with a best PCE of 16.46% was achieved. However, the intermediate phase could not be identified by X-ray diffraction. Moreover, since toluene can wash not only GBL but also DMSO, it may be hard to induce well-defined intermediate phase for reproducible and uniform growth of MAPbI_3 .

Here we report highly reproducible perovskite solar cell via Lewis base adduct of PbI_2 . Oxygen bearing Lewis base and/or iodide anion form adduct with Lewis acid PbI_2 , which is evidenced by infrared spectroscopy. By utilizing volatile characteristics of Lewis base in adduct, a reproducible and facile process is developed, which eventually results in an average PCE of 18.3% from 41 cells and a best PCE of 19.7%.

3.2. Results and discussion

Figure 3.1 shows schematic representation of the fabrication processes that we have studied. 50 wt% DMF solutions containing MAI and PbI_2 (1:1 mol%) and MAI, PbI_2 and DMSO (1:1:1 mol%) are prepared. One-step spin coating at 4000 rpm leads to the rod shaped MAPbI_3 crystals that are not fully covered on the substrate as observed in SEM images (**Figure 3.1a and b**), which is ascribed to different solubility of PbI_2 and MAI. The poor morphology is likely to be induced by difference in crystal growth rate between low solubility PbI_2 and high solubility MAI while DMF is rapidly evaporating. On the other hand, highly densified MAPbI_3 films are formed when the solvent DMF is selectively washed with non-polar diethyl ether while spinning because rapid evaporation problem may be solved by washing. As can be seen in SEM images in **Figure 3.1c and d**, the both solutions produce smooth and homogeneous MAPbI_3 films, but the solution without DMSO leads to pinholes. This indicates that evaporation rate of DMF cannot be perfectly controlled by washing with diethyl ether. Surprisingly, DMSO-contained solution results in the pin-hole-free film (**Figure 3.1d**), which indicates that crystal growth is highly regulated possibly due to adduct $\text{MAI}\cdot\text{PbI}_2\cdot\text{DMSO}$.

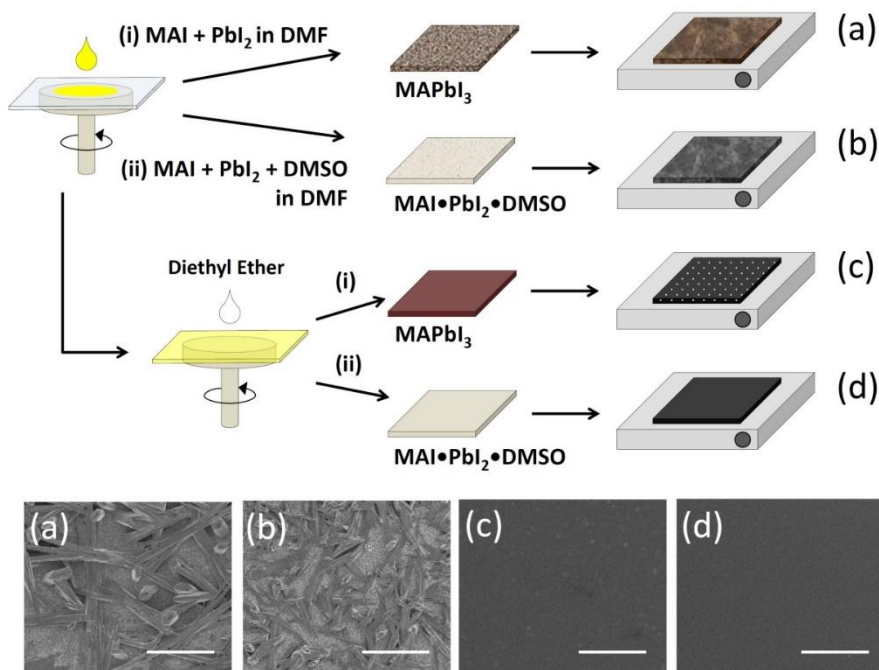


Figure 3.1 Schematic representation of fabrication procedure and plane-view scanning electron microscopy (SEM) images for the MAPbI_3 perovskite layers obtained by direct one-step spin-coating of the DMF solution containing (a) MAI and PbI_2 or (b) MAI, PbI_2 and DMSO. (c) and (d) were prepared by same solution as (a) and (b), but diethyl ether was dripped while the film spinning.

The dark brown MAPbI₃ film shown in **Figure 3.2b** is obtained by heating the transparent film (**Figure 3.2a**) observed right after washing the spin-coated MAI-PbI₂-DMSO layer with diethyl ether. The transparent film is indicative of adduct of PbI₂ with Lewis base DMSO and iodide in MAI. Lewis acid PbI₂ was known to form adduct by reaction with oxygen, nitrogen and sulphur bearing Lewis bases, where lone pair electrons on oxygen in DMSO donates to Lewis acid Pb²⁺ in PbI₂ to form adducts with ratio of PbI₂:DMSO =1:1 and 1:2.[15] Other solvents with oxygen donor such as *N,N*-dimethylacetamide (DMA) and DMF can form adduct with PbI₂, but more stable adduct is expected from DMSO due to stronger polarity (relative polarity of 0.444 for DMSO vs 0.386 for DMF¹⁴). Iodide (I⁻) in MAI is also strong donor and thereby readily forms adduct with PbI₂. It is actually observed that solubility of PbI₂ is more enhanced in the presence of MAI compared to the solubility of PbI₂ dissolved only in DMF, which indicates that I⁻ interacts strongly with PbI₂.

IR spectroscopic study is conducted to investigate adduct formation. **Figure 3.2c** shows IR spectra for liquid DMSO, powdered PbI₂•DMSO and MAI•PbI₂•DMSO (see experimental for details). Stretching vibration of S=O ($\nu(\text{S}=\text{O})$) appears at 1045 cm⁻¹ for the bare DMSO,¹⁵ which is shifted to 1020 cm⁻¹ for PbI₂•DMSO and further shifted to lower wavenumber of 1015 cm⁻¹ for

MAI•PbI₂•DMSO (**Figure 3.2d** and **Table 3.1**). The $\nu(\text{S}=\text{O})$ at 1020 cm^{-1} is well consistent with the frequency of 1022 cm^{-1} observed for the 1:1 adduct of PbI₂•DMSO.[15] According to harmonic motion for diatomic model,¹⁶ frequency of vibration is proportional to square root of force constant. Thus the decreased S=O stretching frequency indicates that force constant is decreased, which is due to decrease in bond strength between sulphur and oxygen as a consequence of the adduct formation. Thus, the S=O stretching frequencies of PbI₂•DMSO and MAI•PbI₂•DMSO are detected in lower wavenumber than that of DMSO. It is noted that the S=O stretching wavenumber for MAI•PbI₂•DMSO is lower than that of PbI₂•DMSO. The S=O bond strength is expected to be more decreased when more Lewis acids are interacted with DMSO.[15] NH₃⁺ stretching peak appears in MAI•PbI₂•DMSO (**Figure 3.2c**), from which the S=O bond strength is further decreased due to more interaction with Lewis acids of MA⁺ and Pb²⁺ ions.

Adduct of PbI₂ with DMSO and MAI is confirmed, as evidence by IR spectroscopic study. Thus, the transparent film in **Figure 3.2a** represents the adduct MAI•PbI₂•DMSO. Regarding the washing solvent, since toluene and chlorobenzene are miscible with DMSO,^{12,17} we have found that diethyl ether is more proper solvent to keep the nominal ratio of MAI:PbI₂:DMSO = 1:1:1 because it

dissolves only DMF and thereby leads to well-defined adduct. Since DMSO in adduct is known to be volatile,[15] the transparent film can be changed to brown MAPbI₃ upon blowing or being exposing to air for a few hours. It was observed that the colorless transparent needle crystal obtained from the saturated solution of DMSO with PbI₂ recovered original yellow color in air due to volatility of DMSO.[14] However, the resulting MAPbI₃ film is found to be inhomogeneous because vaporization of DMSO occurs gradually from the surface of the adduct film. We have found that low temperature heat treatment at 65 °C for 1 min is effective and sufficient to remove entire DMSO from the adduct. Highly dense and homogeneous MAPbI₃ films are eventually obtained by further annealing at 100 °C for 2 min. It is noted that equimolar DMSO plays an important role to form high quality perovskite films since excess DMSO such as PbI₂:MAI:DMSO (1:1:2 mol%) precursor results in extra PbI₂ upon exposing in air (**Figure 3.3**). The adduct-induced MAPbI₃ is found to be quite stable in air atmosphere (**Figure 3.4**)

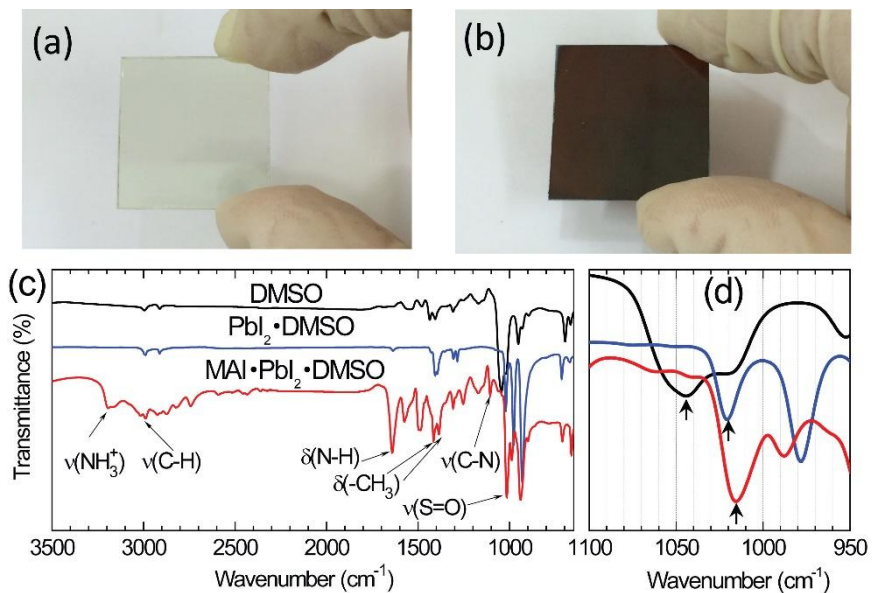


Figure 3.2 Photos of MAPbI₃ on FTO glass (a) before and (b) after annealing at 65 °C for 1 min and 100 °C 2 min. Fourier transform infrared spectrometer (FTIR) of (c) DMSO (solution), PbI₂·DMSO (powder), MAI·PbI₂·DMSO (powder) and (d) expanded the finger print region for the S=O vibrations.

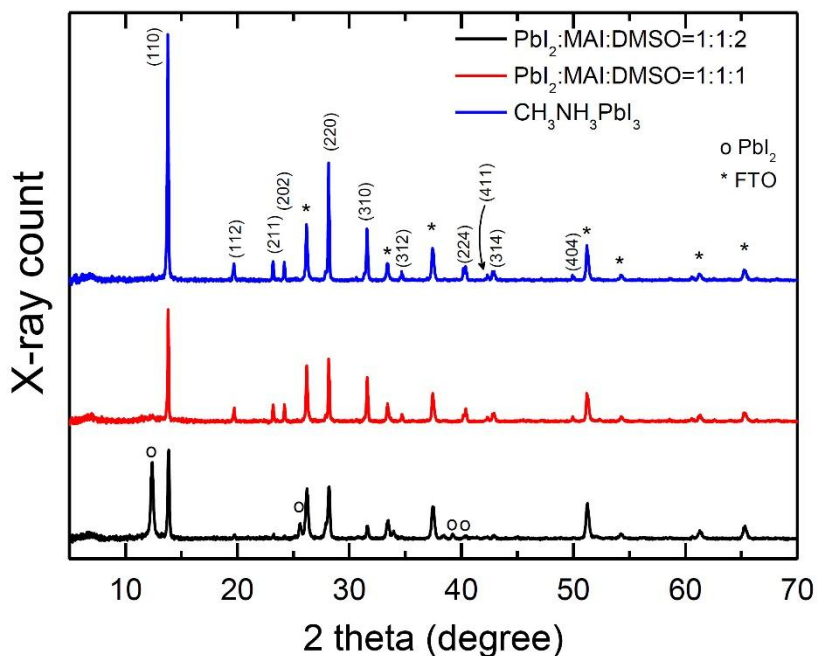


Figure 3.3 X-ray diffraction patterns of perovskite films on FTO glass fabricated by using PbI_2 :MAI:DMSO (1:1:1 mol%, red) and PbI_2 :MAI:DMSO (1:1:2 mol%, black) solutions with diethyl ether treatment. Although both films were not annealed, these were crystallized spontaneously due to volatile DMSO. XRD peaks corresponding to PbI_2 appeared in the case of PbI_2 :MAI:DMSO (1:1:2) contrary to the case of PbI_2 :MAI:DMSO (1:1:1). The XRD pattern (blue) represents perovskite film obtained after heat treatment.

	DMSO	PbI ₂ •DMSO	MAI•PbI ₂ •DMSO
$\nu(\text{S}=\text{O})$	1045 cm ⁻¹	1020 cm ⁻¹	1015 cm ⁻¹

Table 3.1 Stretching frequency of S=O for liquid DMSO and powdered PbI₂•DMSO and MAI•PbI₂•DMSO adducts, along with their chemical structures.

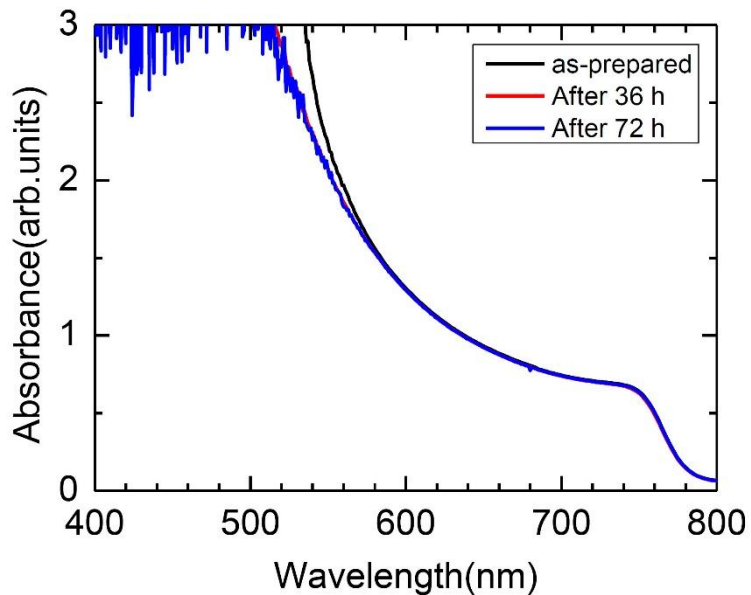


Figure 3.4 UV-visible absorption spectra depending on aging time of the perovskite film prepared by adduct method. The film was stored at ambient conditions (Relative humidity > 45%) without encapsulation and using desiccator.

The charge carrier transport property of the MAPbI₃ prepared via adduct is studied by photoinduced charge extraction by linearly increasing voltage (photo-CELIV)[34] with FTO/bl-Al₂O₃/mp-TiO₂/MAPbI₃/spiro-MeOTAD/Ag configuration (bl and mp stand for blocking and mesoporous). **Figure 3.5** shows the current transient of photo-CELIV for the MAPbI₃ layers prepared via adduct of MAI•PbI₂•DMSO, which is compared with the MAPbI₃ prepared by spin-coating of the DMF solution without DMSO and washing with diethyl ether. Charge carrier mobility is calculated from current (*j*)-time (*t*) curve in **Figure 3.5a**. A charge extraction CELIV peak appears at 3 μs after applying triangular increasing voltage ramp and then current is saturated to the displacement current of the capacitance (*j*₀).^{19,20} The difference in current density arises from difference in film thickness of 650 nm for the adduct-induced MAPbI₃ and 500 nm for the MAPbI₃ without DMSO because *j*₀ is defined as $j_0 = \epsilon\epsilon_0 A/d$ (ϵ : dielectric constant, ϵ_0 : vacuum permittivity, *A*: voltage increase rate, *d*: film thickness).[34,35] The difference in film thickness at the given coating condition is attributed to change in viscosity by DMSO, which affect *j*₀ and entire current density. The charge carrier mobility is calculated by the equation with the current density at maximum peak (Δj) and *t*_{max} that is the time when the current density is maximized.[35] The charge carrier mobility for the

adduct-induced MAPbI₃ is estimated to be $3.9 \times 10^{-3} \text{ cm}^2/\text{Vs}$, which is slightly higher than $2.7 \times 10^{-3} \text{ cm}^2/\text{Vs}$ for the adduct free case (**Table 3.2**). Our sample shows one order of magnitude higher than the MACl-assisted one-step solution growth of MAPbI₃ ($3.2 \times 10^{-4} \text{ cm}^2/\text{Vs}$).²¹ In **Figure 3.5b**, Δj is normalized by j_0 to compare charge extraction behaviour. Extracted charge is proportional to the area of the curve. Extracted charges of the adduct-induced MAPbI₃ are greater than those of the sample without DMSO. The extent of the extracted charges can explain charge recombination. Photoexcited electrons and holes will be extracted by built-in electric field or recombined in the absence of external electric field. Since photo-CELIV is designed to extract charges not by built-in electric field[36,37], the extracted charges in **Figure 3.5b** results from the charges that are not recombined. Therefore the more extracted charges in the adduct-induced MAPbI₃ is indicative of slow recombination.[10]

	Film thickness (nm)	U_{offset} (V)	U_{max} (V)	T_{pulse} (μs)	A (V/s)	T_{max} (μs)	J_0 (mA/cm^2)	J_{max} (mA/cm^2)	Δj (mA/cm^2)	μ (cm^2/Vs)
w/ DMSO	650	-0.72	0.48	20.	60000	3.40	10.90	12.24	1.34	3.89×10^{-3}
w/o DMSO	500	-0.72	0.48	20	60000	3.14	14.14	15.73	1.59	2.71×10^{-3}

Table 3.2. Parameters for photo-CELIV measurements and data obtained from the parameters. Details are found in references 7 and 8.

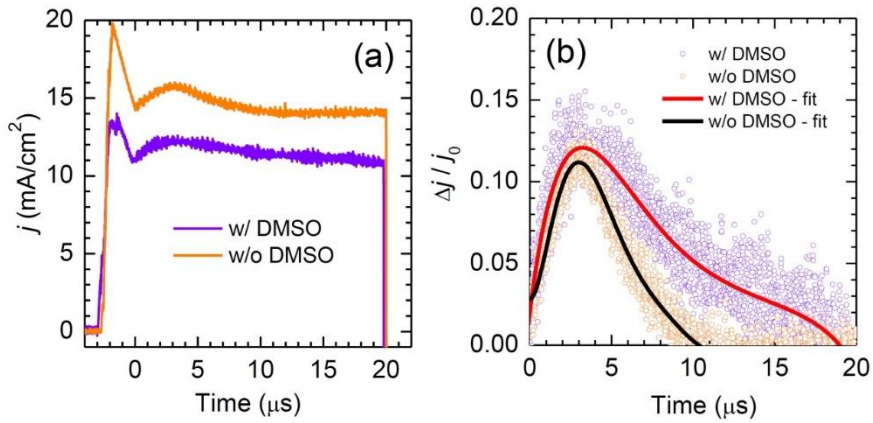


Figure 3.5 (a) The photo-CELIV current transients of perovskite solar cell consist of FTO/bl-Al₂O₃/mp-TiO₂/MAPbI₃/Spiro-MeOTAD/Ag in case of DMF or DMSO/DMF used as solvents for MAPbI₃. (b) The current peaks (Δj) of photo-CELIV current transients normalized by their displacement current of capacitance(j_0), respectively. Curves were fitted by polynomial fitting to compare charge extraction behaviour of sample with or without DMSO.

Figure 3.6 shows photovoltaic performance along with SEM images of the surface of MAPbI₃ and the cross-sectional full cell. The adduct-induced MAPbI₃ shows high dense nature with grains sizing from 200 nm to 300 nm (**Figure 3.6a**). As can be seen in FIB-assisted SEM images for the full cell with FTO/bl-TiO₂/mp-TiO₂/MAPbI₃/spiro-MeOTAD/Ag configuration in **Figure 3.6b**, highly dense MAPbI₃ film with plateau surface is constructed via adduct approach, where ca. 400 nm-thick capping layer is formed on the 230 nm-thick mp-TiO₂ film. The bl-TiO₂ layer and spiro-MeOTAD layer are about 40 nm and 190 nm, respectively. We have tested several solvents except for diethyl ether, but diethyl ether is eventually found to superior to other solvents in terms of reproducibility. The basis for relatively low reproducibility by other solvents such as toluene or chlorobenzene is because MAPbI₃ quality is significantly dependent on dripping amount and/or spinning rate of washing solvent, and difference in solubility between the solvent for washing and the solvent in the precursor solution. Highly reproducible MAPbI₃ films have been obtained using diethyl ether regardless of spin coating condition if one uses enough amount of diethyl ether for dissolving DMF completely. Photovoltaic parameters are gathered from 41 cells and statistically analysed (**Table 3.3**). As can be seen in **Figure 3.6c-f**, the adduct-induced

MAPbI₃ exhibits photovoltaic parameters with small standard deviation, leading to average short-circuit photocurrent density (J_{sc}) of 23.44 ± 0.37 mA/cm², open-circuit voltage (V_{oc}) of 1.070 ± 0.013 V, fill factor (FF) of 0.729 ± 0.019 and PCE of $18.30 \pm 0.71\%$. The best PCE of 19.71% was achieved with J_{sc} of 23.83 mA/cm², V_{oc} of 1.086 and FF of 0.762 (**Figure 3.6g**). The measured J_{sc} is well consistent with the integrated J_{sc} of 22 mA/cm² estimated from IPCE in **Figure 3.6h**. It is noted that maximum IPCE reaches over 91%, which is mainly due to high charge extraction property of the adduct-induced MAPbI₃ and in part due to light reflection by the back Ag electrode. The high photocurrent density approaching 24 mA/cm² is confirmed not to exceed the theoretical maximum value of 26 mA/cm² as estimated by assuming 100% internal quantum efficiency and 5% optical loss from the FTO glass. J - V hysteresis is checked and little hysteresis is found at slow scan rate, where PCE = 18.62% at reverse scan and 18.18% at forward scan showing 2% difference (**Figure 3.7a**). The stabilized PCE is demonstrated by holding the voltage at the maximum power point at a slow scan according to method described elsewhere (**Figure 3.7b**).[38]

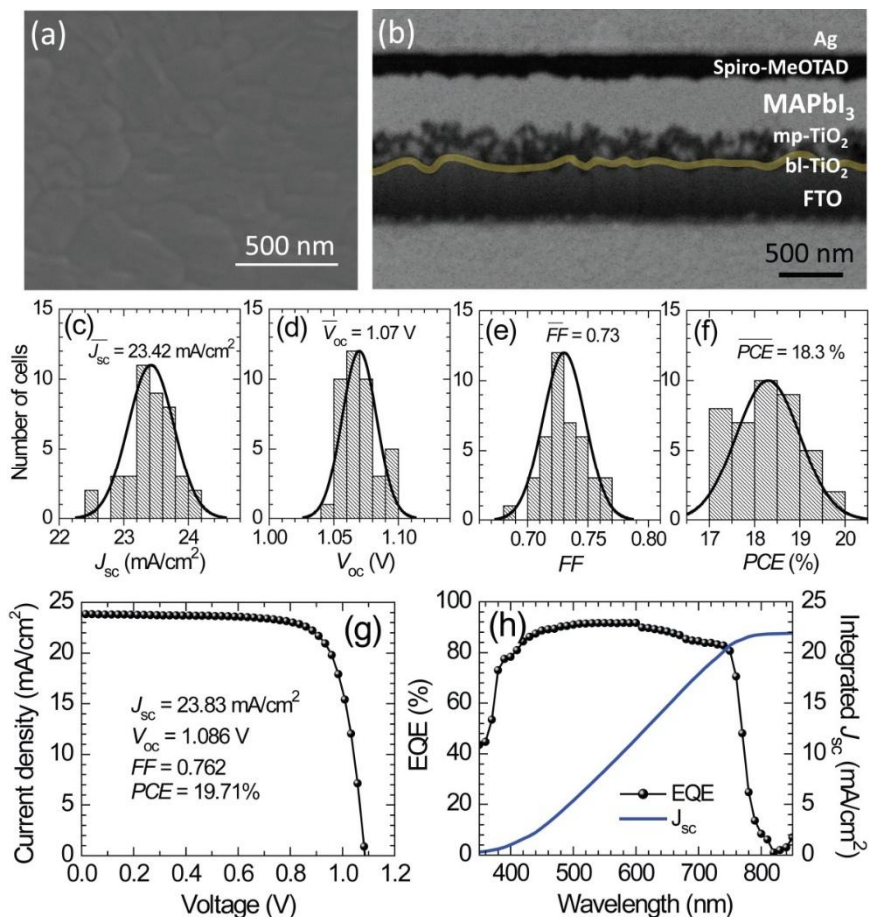


Figure 3.6 (a) Plan-view SEM image of $\text{CH}_3\text{NH}_3\text{PbI}_3$ and (b) FIB-assisted cross sectional SEM image of full cell structure of perovskite solar cell based on the adduct-induced MAPbI_3 . The thickness of bl-TiO_2 , mp-TiO_2 , MAPbI_3 , spiro-MeOTAD and Ag were 40, 200, 400, 200 and 180 nm, respectively. (c)-(f) Histograms of short-circuit current density (J_{sc}), open-circuit voltage (V_{oc}), fill factor (FF) and power conversion efficiency

(PCE) of 41 cells, respectively. (g) J - V curve and (h) external quantum efficiency (EQE) spectrum together with EQE date-based integrated J_{sc} for the best performing perovskite solar cell. J - V data were collected at reverse scan under AM 1.5G one sun illumination (100 mW/cm^2). The aperture mask area was 0.125 cm^2 . The data were collected with the 16 h-aged cells because Ag electrode-based device showed normally poor fill factor right after fabrication.

Device #	J_{sc} (mA/cm ²)	V_{oc} (V)	FF	PCE (%)
1	23.18	1.093	0.721	18.28
2	23.70	1.097	0.730	18.98
3	23.66	1.086	0.735	18.89
4	23.43	1.092	0.727	18.60
5	23.34	1.097	0.735	18.82
6	24.14	1.090	0.728	19.18
7	23.65	1.074	0.723	18.37
8	23.52	1.077	0.732	18.55
9	24.03	1.047	0.679	17.08
10	23.47	1.051	0.717	17.69
11	23.18	1.051	0.724	17.64
12	22.45	1.064	0.718	17.16
13	22.98	1.061	0.714	17.41
14	22.95	1.060	0.713	17.35
15	23.80	1.065	0.723	18.32
16	23.63	1.072	0.745	18.88
17	23.48	1.071	0.726	18.28
18	23.53	1.054	0.732	18.15
19	23.56	1.061	0.732	18.30
20	22.49	1.059	0.744	17.73
21	23.67	1.070	0.683	17.30
22	23.35	1.068	0.700	17.45
23	23.22	1.078	0.755	18.91
24	23.25	1.059	0.745	18.34
25	23.69	1.057	0.723	18.10
26	23.21	1.065	0.724	17.9
27	23.18	1.067	0.727	17.99
28	22.88	1.058	0.718	17.40
29	23.57	1.064	0.730	18.31
30	23.53	1.067	0.716	17.99
31	23.41	1.069	0.727	18.19
32	23.33	1.073	0.743	18.60
33	23.36	1.078	0.758	19.09
34	24.08	1.077	0.744	19.30
35	23.83	1.079	0.750	19.29

36	23.83	1.086	0.762	19.71
37	23.32	1.068	0.763	19.01
38	23.83	1.086	0.762	19.71
39	23.73	1.064	0.747	18.87
40	23.24	1.056	0.704	17.29
41	23.29	1.050	0.727	17.79
Standard deviation	0.367	0.013	0.019	0.708

Table 3.3. Standard deviation of photovoltaic parameters and power conversion efficiency (PCE) for 41 perovskite solar cells based on the adduct-induced MAPbI₃. Average J_{sc} , V_{oc} , FF and PCE were 23.44 mA/cm², 1.070 V, 0.729 and 18.30%, respectively.

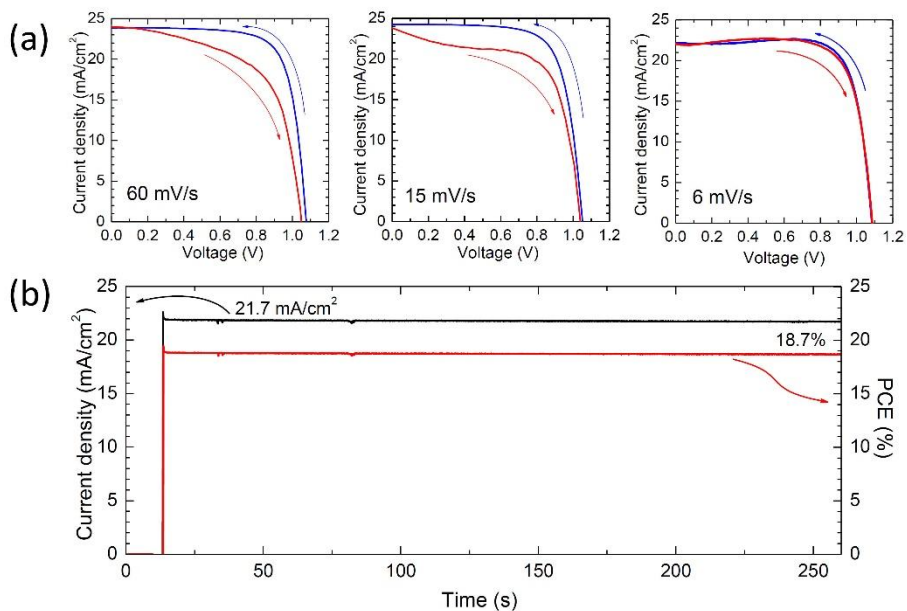


Figure 3.7 (a) J-V curves measured depending on scan direction and scan rate. Measurement from V_{oc} to J_{sc} is referred to reverse scan (blue) and visa versa is forward scan (red). Photovoltaic parameters are listed in Table S3. (b) Stabilized photocurrent density (black) and power conversion efficiency (red) measured at maximum power voltage of 0.86V for 250 seconds.

3.3. Conclusions

Highly reproducible perovskite solar cells were fabricated via Lewis base adduct of PbI_2 . 1:1:1 adduct of $\text{MAI}\cdot\text{PbI}_2\cdot\text{DMSO}$ was formed by spin-coating of the DMF solution containing equimolar MAI, PbI_2 and DMSO and using diethyl ether to remove solvent DMF only. We achieved average PCE of 18.3% and best PCE of 19.7% by the adduct chemistry. Studies on materials, device structures and chemical engineering of interfaces are expected to further improve the solar cell efficiency using the adduct-induced perovskite light absorber.

3.4. Experimental method

Preparation of materials

CH₃NH₃I. Meththylammonium iodide (CH₃NH₃I) was synthesized according to method reported elsewhere [1-3]. Methylamine (27.8 ml, 40 wt% in methanol, TCI) was reacted with hydroiodic (30 ml, 57 wt% in water, Aldrich) at 0 °C for 2 h. CH₃NH₃I was recovered by rotary evaporation at 50 °C for 1 h. The product was washed with diethyl ether and dried in vacuum oven at 60 °C for 24 h.

PbI₂•DMSO adduct. 461 mg of PbI₂ (99.9985%, Alpha Aesar) was dissolved in 2 ml of N,N-dimethylsulfoxide (DMSO, 99.5%, Sigma-Aldrich) and anhydrous ethanol was added to the solution. The precipitation was filtered and dried in vacuum oven for 1 h, which was used for infrared (IR) spectroscopy measurement.

CH₃NH₃I•PbI₂•DMSO adduct. 461mg of PbI₂, 159 mg of CH₃NH₃I and 78 mg of DMSO were mixed in 600 mg of N,N-dimethylformamide (DMF, 99.8%, Sigma-Aldrich). Diethyl ether was added to the fully-dissolved solution. The precipitate was filtered and dried in vacuum oven for 1 h, which was uded for IR spectroscopy measurement.

Solar cell fabrication

FTO glasses (Pilkington, TEC-8, 8Ω/sq) was cleaned with detergent, dilluted water, and acetone and sonicated with ethanol in

an ultrasonic bath for 20 min. UVO was treated for 15 min prior to use. To prepare the TiO₂ blocking layer (bl-TiO₂), 0.15 M titanium diisopropoxide di(acetylacetonate) (Sigma-Aldrich, 75 wt% in isopropanol) in 1-butanol (Sigma-Aldrich, 99.8%) was spin-coated on a FTO glass substrate at 700 rpm for 8 sec, 1000 rpm for 10 sec and 2000 rpm for 40 sec, which was followed by drying at 125 °C for 5 min. Mesoporous TiO₂ (mp-TiO₂) layer was deposited on the bl-TiO₂ by spin-coating the TiO₂ colloidal solution containing 1.2 g of TiO₂ paste (50nm sized nanocrystalline TiO₂, terpeneol, ethylcellulose and lauric acid with a nominal ratio of 1.25: 6 : 0.9 : 0.3 in wt%) diluted in 10 ml of anhydrous ethanol solution at 2000 rpm for 20 sec, which was annealed at 550 °C for 1 h and then UVO was treated for 15 min. The substrate was further treated with 20 mM aqueous TiCl₄ (Sigma-Aldrich, > 98%) solution at 90 °C for 10 min, cleaned with deionized water and then sintered at 500°C for 30 min. 461 mg of PbI₂, 159 mg of CH₃NH₃I, and 78 mg of DMSO (molar ratio 1:1:1) was mixed in 600 mg of DMF solution at room temperature with stirring for 1 h in order to prepare a CH₃NH₃I•PbI₂•DMSO adduct solution. The completely dissolved solution was spin-coated on the mp-TiO₂ layer at 4000 rpm for 25 sec and 0.5 ml of diethyl ether was slowly dripped on the rotating substrate in 10 sec before the surface changed to be turbid caused by

rapid vaporization of DMF. The transparent $\text{CH}_3\text{NH}_3\text{I}\cdot\text{PbI}_2\cdot\text{DMSO}$ adduct film was heated at 65°C for 1 min and 100°C for 2 min in order to obtain a dense $\text{CH}_3\text{NH}_3\text{PbI}_3$ film. The 20 μl of spiro-MeOTAD solution, which was consisted of 72.3 mg spiro-MeOTAD (Merck), 28.8 μl of 4-tert-butyl pyridine and 17.5 μl of lithium bis(trifluoromethanesulfonyl)imide (Li-TFSI) solution (520 mg Li-TFSI in 1 ml acetonitrile (Sigma–Aldrich, 99.8 %) in 1ml of chlorobenzene, was spin-coated on the perovskite layer at 3000 rpm for 30 sec. Finally, Ag electrode was deposited by using thermal evaporator at a constant evaporation rate of 0.03 nm/s.

Characterizations

The surface images of perovskite film was obtained from a field emission scanning electron microscope (FE-SEM, Auriga, Carl Zeiss) and a focused-ion beam assisted SEM (FIB-SEM) was used to investigate the cross-sectional images of perovskite solar cells. A Fourier transform infrared spectroscopy (FT-IR, Nicolet 6700, Thermo Scientific) was used to collect the FT-IR spectral data for DMSO (liquid phase), $\text{PbI}_2\cdot\text{DMSO}$ adduct, and $\text{CH}_3\text{NH}_3\text{I}\cdot\text{PbI}_2\cdot\text{DMSO}$ adduct in the 4000 cm^{-1} - 650 cm^{-1} range. The KBr pellet was used for the powdered samples of $\text{PbI}_2\cdot\text{DMSO}$ and $\text{CH}_3\text{NH}_3\text{I}\cdot\text{PbI}_2\cdot\text{DMSO}$ adducts. The absorption spectra were recorded using UV/Vis spectrometer (Lambda 45, Pelkin Elmer) in

the 400 nm -900 nm range. Photocurrent density-voltage (J-V) curves were measured under AM 1.5G one sun illumination (100 mW/cm^2) with a solar simulator (Oriel Sol 3A class) equipped with 450 W Xenon lamp (Newport 6279NS) and a Keithley 2400 source meter. The light intensity was adjusted by NREL-calibrated Si solar cell having KG-2 filter. While measuring, the cell was covered with a mask having an aperture (0.125 cm^2). The Ag electrode based solar cells were measured after aging for 16 h. In order to demonstrate that the efficiency is stable for at least a minute, photocurrent density and PCE were measured at maximum power voltage for 250 s. External quantum efficiency (EQE) was measured using an EQE system (PV measurement Inc.) under DC mode, where a 75W Xenon lamp (USHIO, Japan) was used a light source for generating monochromatic beam.

Photo-CELIV measurements

To investigate mobility and charge extraction characteristics, photo-CELIV (Charge Extraction by Linearly Increasing Voltage) transients were recorded for the devices with FTO/bl- Al_2O_3 /mp- TiO_2 / $\text{CH}_3\text{NH}_3\text{PbI}_3$ /spiro-MeOTAD/Ag configuration (bl and mp represent blocking and mesoporous) in ambient air condition. In order to collect hole only, Al_2O_3 blocking layer (bl- Al_2O_3) was used for blocking electron collection. Nd:YAG (MINILITE I, Continuum;

532 nm, 12 mJ/pulse, pulsewidth = 3~5 ns) illuminated to FTO side of the sample. After 3 μ s delay linearly increasing voltage pulse generated by function generator (DS345, Stanford Research Systems) was applied to the samples in reverse bias (positive probe was connected to the FTO and negative probe was connected to the Ag electrode). Offset voltage (U_{offset}) for suppression charge extraction by built-in electric field was -0.72 V and maximum voltage was 0.48 V for 20 μ s. Current transient was monitored by converting voltage measured by digital oscilloscope (TDS3054B, Tektronix) using a 50 Ω load resistor . Charge carrier mobility was calculated according to Equation (1),

$$\mu = \frac{2d^2}{3At_{\text{max}}^2 \left[1 + 0.36 \frac{\Delta j}{j_0} \right]} \quad \text{if } \Delta j \leq j_0 \quad (1)$$

where d is the film thickness, A is the voltage increase rate, t_{max} is the time at maximum Δj of the extraction peak and j_0 is the capacitive displacement current. To investigate amount of extracted charges, Δj was normalized by j_0 $\Delta j / j_0$ data were fitted by polynomial curve fitting.

Chapter 4.

Compositional Perovskite Systems with Cubic Structure for Long-Term Stability

Published in *Nature Communications*, 2016, 7, 13422

4.1. Introduction

Organic inorganic hybrid perovskites have been attracting worldwide interest as a low-cost alternative of conventional photovoltaic materials such as silicon (Si), copper indium gallium selenide (CIGS), and gallium arsenide (GaAs). The power conversion efficiency (PCE) of perovskite based solar cells has already exceeded 20%^[6], which is favorably compared with commercial crystalline Si solar cells. Their long-term stability, however, is rather poor such that typical perovskite solar cells can only last from a few hours to a few days even with encapsulation^[39]. In order for perovskite photovoltaic technologies to be commercially viable, it is crucial to achieve long-term stability at least over 10 years, considering that the lifespan of current commercial photovoltaic modules are over 20 years.

The most widely used perovskite material, $\text{CH}_3\text{NH}_3\text{PbI}_3$ (MAPbI₃), which possesses excellent electrical and optical properties

for photovoltaic applications, is unstable to heat and light[17]. This is partly due to its structural instability: the Goldschmidt tolerance factor of MAPbI₃ is 0.84 and thus it forms structurally distorted tetragonal crystals. The crystal structure of perovskite can become more stable by increasing the tolerance factor close to unity by incorporating other organic cation and halide anion with different ion sizes. Addition of formamidinium (FA) cation and bromide (Br) anion not only structurally stabilize the perovskite materials by inducing cubic crystals, but also enhance their photovoltaic performance. Although several studies on mixed cation and/or halide anion system of MA_xFA_{1-x}PbI_yBr_{3-y} have been already suggested[5,6], comprehensive optimization of both stability and performance is still required.

In this work, we simultaneously optimize the perovskite material and the device structure to be stable, efficient, hysteresis-less, and low-temperature processable. We developed highly efficient and stable mixed compositional MA_{0.6}FA_{0.4}PbI_{2.9}Br_{0.1} perovskite formed via lewis-base adduct method. MA_{0.6}FA_{0.4}PbI_{2.9}Br_{0.1} perovskites were more stable than MAPbI₃ perovskites not only under high humidity in dark condition but also under one sun illumination in ambient air. Moreover, by substituting FTO/TiO₂ with ITO/C₆₀, we obtained the low-temperature processable cells with the best PCE of 20.2% and the average PCE of 19.12% with no hysteresis.

4.2. Results and discussion

In a mixed cation and halide anion system of Pb-based perovskite, APbX₃, the Goldschmidt tolerance factor t is defined in terms of the average radii of ions as follows.

$$t = \frac{\overline{r_A} + \overline{r_X}}{\sqrt{2}(\overline{r_{Pb}} + \overline{r_X})} \text{ (Equations 1)}$$

where $\overline{r_A}$, $\overline{r_X}$, and $\overline{r_{Pb}}$ are the average radii of the cation, anion, and lead ions, respectively. The I⁻, Br⁻ and Pb²⁺ ions have a spherical shape and the radii of these ions have been measured in the previous work[40]. In contrast, it is difficult to precisely estimate the radii of the organic cations perched on the A site due to their non-spherical shape and rotational motion, nevertheless, several groups already reported the calculated effective ion radius of both MA⁺ and FA⁺ cation[41-44]. By using equation 1 and the suggested ionic radii ($r_{MA^+} = 0.18$ nm, $r_{I^-} = 0.22$ nm, $r_{Pb^{2+}} = 0.12$ nm), the tolerance factor of MAPbI₃ is calculated to be 0.83⁵, indicating that MA⁺ cations are too small to fit into the interstices between PbX₆ octahedra. This mismatch causes crystal distortion, and consequentially MAPbI₃ perovskite have unstable tetragonal crystal structure [45,46]. By partially replacing MA⁺ and I⁻ to relatively larger FA⁺ and smaller Br⁻ ions respectively, crystal distortion can be alleviated to produce more stable cubic structure with the tolerance factor between 0.9-

1[18]. Simple calculation reveals that replacing I- to Br- ($r_{Br^-} = 0.196$ nm) only marginally affects the perovskite crystal structure as the tolerance factor of $MAPbBr_3$ is only 0.01 higher than that of $MAPbI_3$. On the other hand, replacing MA to FA cation can significantly alter the crystal structure because FA cations are expected to be much larger than MA cations. The exact radius of FA cation is still controversial[18,47], but considering that $FAPbI_3$ can possess not only non-perovskite yellow δ -phase with hexagonal crystal structure ($t > 1$) but also black perovskite α -phase with cubic structure ($0.9 < t < 1$), it can be speculated that the tolerance factor of $FAPbI_3$ would be around 1. The radius of FA cation r_{FA^+} is estimated to be around 0.26 nm from these speculations and equation 1. The tolerance factor of mixed cation system, $MA_xFA_{1-x}PbI_3$, is calculated as a function of the ratio x as shown in **Figure 4.1**. This relation suggests that the x values between 0.2 and 0.6 lead to the most stable cubic crystal structure, as the resulting tolerance factor lies between 0.9 and 1.

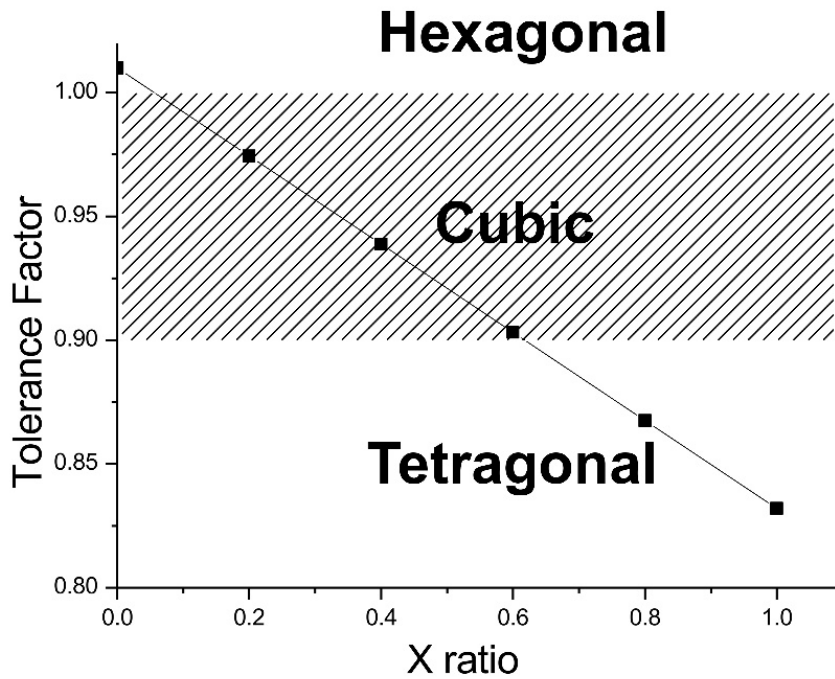


Figure 4.1 Dependence of the Goldschmidt tolerance factor on the MA fraction (x) of $\text{MA}_x\text{FA}_{1-x}\text{PbI}_3$. Dashed zone means region for cubic structure ($0.9 < t < 1$).

We measured X-ray diffraction(XRD) patterns of five types of mixed perovskite films ($x= 1, 0.8, 0.6, 0.4, 0.2$) coated on the ITO glass in order to compare their stability. **Figure.4.2a,b** show the XRD patterns of the fresh and degraded samples, respectively. The perovskite films were degraded in the chamber (relative humidity (RH) $\sim 50\%$) for 10 hours under one sun illumination. The peak originating from PbI_2 at 12.7 degrees intensively appears in the case of MAPbI_3 ($x=1$), and the peak of non-perovskite δ -phase FAPbI_3 at 11.7 degrees appears for $x < 0.4$, which indicates severe instability to water vapor[48]. (**Figure.4.2c and d**) These observations suggest that the most stable composition would be $\text{MA}_{0.6}\text{FA}_{0.4}\text{PbI}_3$ ($x=0.6$), which still possesses the tolerance factor ensuring the cubic crystal structure.

We also fabricated the full devices with the ITO/ C_{60} /Perovskite/Spiro-MeOTAD/Au structure in order to find the optimal composition with respect to the photovoltaic performances in mixed perovskite $\text{MA}_x\text{FA}_{1-x}\text{PbI}_y\text{Br}_{3-y}$. **Figure.4.3a and b** summarize the PCEs as a function of the MA+ fraction(x) and the Br- fraction($3-y$), respectively. As a result, the $\text{MA}_{0.6}\text{FA}_{0.4}\text{PbI}_{2.9}\text{Br}_{0.1}$ -based devices were shown to the best performance. Considering that MA:FA=0.6:0.4 is the best composition for stability, we concluded

that $\text{MA}_{0.6}\text{FA}_{0.4}\text{PbI}_{2.9}\text{Br}_{0.1}$ would be the best composition in terms of both performance and stability in mixed perovskite systems.

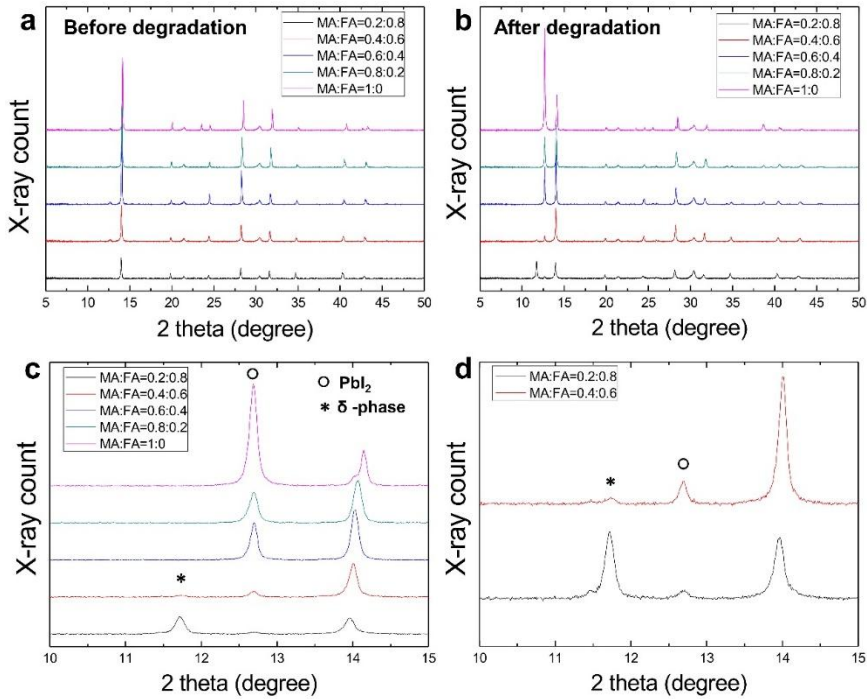


Figure 4.2 X-ray diffraction patterns of five different mixed perovskite films coated on ITO glass ($x=0.2$ (black), 0.4 (red), 0.6 (blue), 0.8 (green), and 1 (pink)) (a) before and (b) after degradation under one sun illumination at 50 % relative humidity for 10 hours. (c) Magnified XRD patterns around the peaks originating from PbI_2 and non-perovskite δ -phase. (d) Magnified XRD patterns for $x=0.2$ and 0.4 .

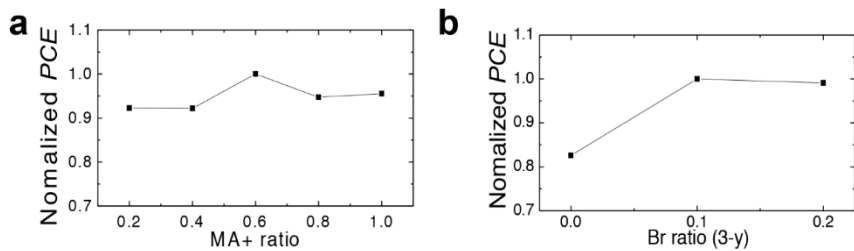


Figure 4.3 Dependence of the normalized PCEs of ITO/C₆₀/Perovskite/Spiro-MeOTAD /A device on (a) the MA+ fraction (x), and (b) the Br- fraction (3-y).

Another intriguing experimental observation is the light soaking in the presence of moisture, which consistently showed irreversible degradation of perovskite in previous works[17,21,49], whereas in the dark condition moisture introduction only formed reversible hydrates of perovskites, for example, $\text{CH}_3\text{NH}_3\text{PbI}_3 \cdot \text{H}_2\text{O}$ or $(\text{CH}_3\text{NH}_3)_4\text{PbI}_6 \cdot 2\text{H}_2\text{O}$ [49,50]. The reason has not been elucidated yet, although Christians *et al.*[49] suggested that organic cation could become less tightly bound to PbI_6^{4-} octahedra after light soaking. The charge generation under light soaking and subsequent trapping on the surface of perovskite is suspected to influence the stability (It will be discussed in Chapter 5). **Figure 4.4** showed the degradation behaviour of MAPbI_3 and our mixed $\text{MA}_{0.6}\text{FA}_{0.4}\text{PbI}_{2.9}\text{Br}_{0.1}$, respectively, for 2 days in the dark condition with relative humidity (RH) 90%. Absorption spectra measurements show that the original MAPbI_3 (black curve) became hydrated (red curve) after 2 days and then dehydrated reversibly via N_2 drying, which is consistent with previous studies[49,50]. On the other hand, the absorption spectra of our mixed $\text{MA}_{0.6}\text{FA}_{0.4}\text{PbI}_{2.9}\text{Br}_{0.1}$ perovskite were hardly changed with the same condition (see **Figure.4.4d**). This indicates our mixed composition perovskite would be more resistible to become hydrated than distorted tetragonal perovskite MAPbI_3 . It is likely to be that water molecules could penetrate more easily into the distorted

tetragonal MAPbI₃ than into the more compact cubic crystal structure of MA_{0.6}FA_{0.4}PbI_{2.9}Br_{0.1}. A slight change of the absorption spectra shown in **Figure 4.4d** indicates a slow hydration could still happen to our mixed perovskite under 90% RH. However, both perovskites showed irreversible degradation rapidly under light soaking even at low RH 20% (see **Figure 4.4g-l**), which is also consistent with previous report[49,51]. It is interesting to note that under light soaking, our mixed perovskite degrades more slowly than the conventional MAPbI₃.

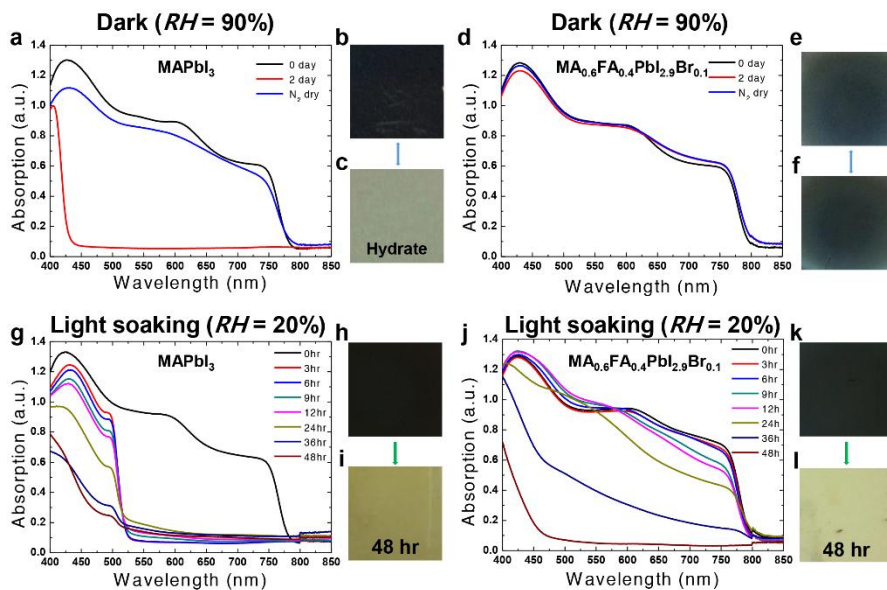


Figure 4.4 (a) Absorption spectra and pictures of the MAPbI₃ perovskite film (b) before and (c) after ageing for 2 days under dark conditions at 90% RH. MAPbI₃ perovskites were transformed into transparent hydrated states after 2 days. (d) Absorption spectra and pictures of the MA_{0.6}FA_{0.4}PbI_{2.9}Br_{0.1} perovskite film (e) before and (f) after ageing under the same condition. (g) Time evolution of absorption spectra and pictures of MAPbI₃ (h) before and (i) after degradation under light soaking at 20% RH. (j) Time evolution of absorption spectra and pictures of MA_{0.6}FA_{0.4}PbI_{2.9}Br_{0.1} (k) before and (l) after degradation under the same condition.

Finally, the solar cells employing the MA_{0.6}FA_{0.4}PbI_{2.9}Br_{0.1} perovskite films were fabricated and characterized. (ITO/C₆₀/perovskite/Spiro-MeOTAD/Au).

Figure.4.5a shows J - V curves for the device measured at various sweep delay, which demonstrates sweep rate-independent and hysteresis-less performance of the best PCE of 20.2%. The best PCE value was averaged from the J - V curves of forward and reverse scan, which is in agreement with 20.2% of steady-state efficiency shown in **Figure.4.5b**. The integrated J_{sc} estimated from external quantum efficiency (EQE) was also well-matched with the measured J_{sc} as shown in **Figure.4.5c**. Histograms of the short-circuit current (J_{sc}), the open-circuit voltage (V_{oc}), the fill factor (FF) and the efficiency of 47 cells are shown in **Figure4.5d-g**. The photovoltaic characteristics of these cells were highly reproducible with a small standard deviation, and the average values are $J_{sc} = 24.34 \text{ mA cm}^{-2}$, $V_{oc} = 1.058 \text{ V}$, $FF = 0.743$, and $PCE = 19.12\%$, respectively. This would be the best performance of low-temperature processed perovskite solar cells without using mesoporous TiO₂.

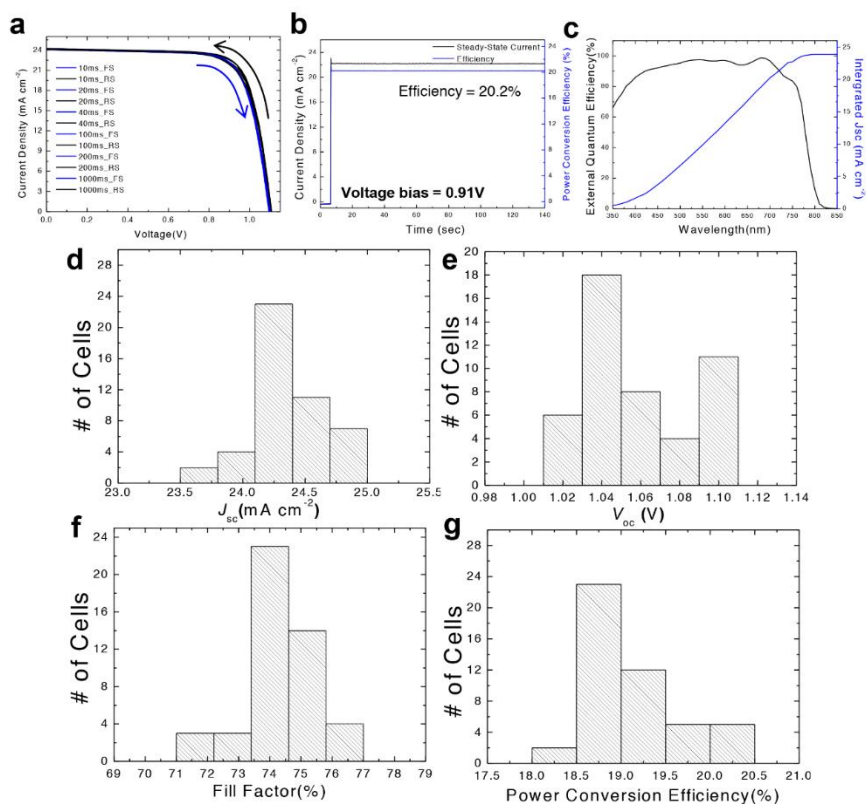


Figure 4.5 Photovoltaic performance characteristics. (a) J - V curves of the best-performing device measured at various sweep delay times. (b) Stabilized photocurrent density (black) and power conversion efficiency (blue) measured at a bias voltage of 0.91V for 140 seconds. (c) External quantum efficiency (EQE) spectrum and the integrated J_{sc} estimated from the measured EQE. Histograms of (d) short-circuit current density (J_{sc}), (e) open-circuit voltage (V_{oc}), (f) fill factor (FF), and (g) power conversion efficiency (PCE) of 47 cells

4.3. Conclusion

We have demonstrated that new mixed-perovskite solar cells based on $\text{FA}_{0.4}\text{MA}_{0.6}\text{PbI}_{2.9}\text{Br}_{0.1}$, whose composition is engineered to minimize the crystal distortion, exhibit improved photovoltaic performance and stability compared to widely-used MAPbI_3 based devices. These cells incorporate C_{60} as ETL, which is advantageous over TiO_2 due to low-temperature processability, absence of hysteresis, and enhanced device stability. As a result, our best device have shown the PCE of 20.2%, the highest efficiency of all low-temperature processed perovskite solar cells.

4.4. Experimental method

Mixed perovskite film fabrication

All perovskite films were fabricated by spin-coating of precursor solution. The precursor solutions were prepared by dissolving 1mmol of (MAI+ FAI + MABr), 1mmol of PbI₂ and 1mmol of DMSO in 0.55 ml of dimethylformamide (DMF). To compare different compositional perovskites, the amounts of MAI, FAI and MABr were adjusted.

Solar cell fabrication

ITO glass substrates (AMG, $9.5\Omega\text{ cm}^{-2}$, $25 \times 25\text{ mm}^2$) were sequentially sonicated in acetone, isopropanol and deionized water. The cleaned substrate was sufficiently dried in an oven, to eliminate all residual solvents. A 35 nm-thick C₆₀ layer⁴³ was densely coated on the ITO glass substrates by using a vacuum thermal evaporator at the constant rate of 0.1 \AA s^{-1} .^[52] The 50 wt% mixed perovskite solutions (MAI+FAI+MABr : PbI₂ : dimethyl sulfoxide=1:1:1 in dimethylformamide (DMF) solvent) were coated on the ITO/C60 substrate by Lewis base adduct method²⁵. To prepare our best compositional solution, 461 mg of PbI₂, 79.5 mg of MAI, 68.8 mg of FAI, 11.2 mg of MABr and 78 mg of dimethyl sulfoxide were mixed in 0.55 ml of dimethylformamide (DMF) at room temperature with stirring for 30 min. After spin coating at 4,000 r.p.m. for 20 s with

ether dripping treatment, the transparent adduct films were annealed at 130 °C for 20 min, to form black perovskite films. To prepare the HTM, 72.3 mg of Spiro-MeOTAD (Merk) dissolved in 1 ml Chlorobenzene (Sigma-Aldrich) with 28.8 μ l of 4-tert-butyl pyridine and 17.5 μ l of lithium bis (trifluoromethanesulfonyl) imide solution (520 mg lithium bis (trifluoromethanesulfonyl) imide in 1 ml acetonitrile (Sigma-Aldrich, 99.8%)). The HTM solutions were spin coated onto the perovskite layer at 2,000 r.p.m. for 30 s. After all process, 50 nm gold (Au) as a counter electrode was deposited on the HTM at the rate of 0.3 \AA s^{-1} by using a vacuum thermal evaporator. All spin coating processes in our experiments were carried out in a dry room (RH <15%, room temperature).

Chapter 5.

Trapped-Charge Driven Degradation of Perovskite Solar Cells

Published in *Nature Communications*, 2016, 7, 13422

5.1. Introduction

Organic inorganic hybrid perovskite solar cells have shown unprecedented performance increase up to 22% efficiency[7] and are now considered not only as a low-cost alternative to commercialized solar cells[53] but also as a functional cell with flexible applications[54,55]. However, their long-term stability has not been solved yet and this issue is the most pressing problem for commercialization[17]. It is well known that perovskite materials are vulnerable to the exposure of humidity and light[21,22,51]. Although many efforts to encapsulate the devices for preventing direct contact to humidity have been attempted, it was not successful to obtain long-term stability comparable to commercial photovoltaic devices[22]. Various factors that can affect the stability have been investigated from the viewpoints of chemical structure[56], electrical stress[57], hydrated states[21,49,50] and heat[58]. However, the degradation mechanism is still unclear how a fully fabricated device

deteriorates rapidly, even though its perovskite layer is tightly covered by the hole transport material (HTM) and the back electrode. It is also elusive why light soaking causes irreversible degradation of perovskite materials in the presence of moisture, whereas the moisture in the dark condition only induces reversible hydration of perovskite materials[49,50].

The device structure and the choice of charge extraction materials also influence the stability[59]. The use of inorganic charge extraction layers was reported to enhance stability[60]. Other studies have focused on eliminating the pathway of water vapour infiltration into the perovskite film by coating carbon-based materials, polymers and hydrophobic materials on the top surface of the perovskite film[61]. These approaches provide the device lifespan longer than the case without these materials, but not long enough to ensure long-term stability. Such approaches also occasionally sacrifice the photovoltaic performance. Especially, the devices employing titanium dioxide (TiO_2) as electron transport layer (ETL) are rapidly degraded under light soaking[48], even though they are highly efficient in energy conversion and exhibit the world's best efficiency. In the present study, we found the fundamental mechanism for irreversible degradation of perovskite materials in which trapped charges regardless of the polarity play a decisive role. A novel experimental setup utilizing different polarity ions revealed that

the moisture induced irreversible dissociation of perovskite materials is triggered by charges trapped along grain boundaries. We also identified the synergetic effect of oxygen on the process of moisture induced degradation. The deprotonation of organic cations by trapped charge induced local electric field would be attributed to the initiation of irreversible decomposition.

5.2. Results and discussion

First, we examined how solar cell degradation behavior becomes different depending on different charge extraction layers, for example, C_{60} and compact TiO_2 . **Figure.5.1a and b** show $J-V$ curves for $MA_{0.6}FA_{0.4}PbI_{2.9}Br_{0.1}$ perovskite on the C_{60} ETL (a) and compact TiO_2 layer (b), respectively. As shown in **Figure.5.1c,d**, non-encapsulated C_{60} based cell shows much more stable performance under one sun illumination but still degrades while compact TiO_2 based non-encapsulated cell completely died only after 6 hours. To examine the detailed evolution of degradation, we investigated how the cross sectional morphology of the C_{60} and TiO_2 based devices would evolve under illumination via the focused ion beam (FIB) assisted scanning electron microscope (SEM) images shown in **Figure5.2**. Consistent with the PCE measurement results, the SEM images clearly confirm that the C_{60} -based devices are much slowly degraded compared to the TiO_2 -based cells. Strikingly, they showed different degradation patterns, namely, different side of degradation beginning where the degradation is initiated depending on different ETLs. Such degradation pattern is the same for conventional $MAPbI_3$ perovskite (see **Figure.5.3**). Since the reactants that can decompose perovskite materials could infiltrate from the thin metal electrode rather than from the thick ITO glass, it would be expected that the

degradation should be initiated at the interface closer to the thin Au metal electrode. However, the perovskite films of TiO₂-based devices began to be decomposed at the interface adjacent to the compact TiO₂ layer near FTO glass (**Figure.5.2b**). Although these observations were attributed to UV light induced photocatalytic effect of TiO₂ layer according to the previous report[62], we confirmed that the same degradation pattern happened in the TiO₂ and C₆₀ based devices aged even under UV-filtered light illumination (**Figure.5.4**). For those of C₆₀-based devices, the decomposition began from the interface adjacent to HTL near Au metal electrode opposite to the case of TiO₂ based devices. Since the two types of devices have identical structure except for the ETL, C₆₀ or TiO₂/Perovskite/Spiro-MeOTAD/Au, these different degradation characteristics indicate that charge extraction may play an important role where moisture driven decomposition of perovskite material begins. Second, the TiO₂ based devices suffer from severe hysteresis, whereas the C₆₀ based devices do not. Considering that the origin of hysteresis is known as capacitive current[23], trapped charge[63] and unbalanced charge injection[64], many electrons may be accumulated near the ETL in the TiO₂ based devices, while the C₆₀ based devices hardly do. From the observation on the degradation of the TiO₂ based devices that begins from the interface contacting TiO₂

layer where many charges could be trapped, it is reasonable to suspect that trapped charges at the interface between perovskite and charge extraction layer would be responsible for initiating the moisture related decomposition. Fast extraction of electrons through C_{60} would hardly accumulate negative charges at the interface between perovskite and C_{60} , but hole extraction through Spiro-MeOTAD could be slower than the rate of electron extraction in the C_{60} based cell[65,66]. This could result in positive charge trapping at the interface between perovskite and hole extraction layer, which could be the cause why the degradation begins from the interface between perovskite and Spiro-MeOTAD for C_{60} based cells (see **Figure5.2a**). These results demonstrating the degradation beginning from opposite side for different charge extraction layers gave us a clue about the trapped charge driven degradation regardless of polarity. It could be hypothesized that these trapped charges generated under light soaking would be responsible for irreversible degradation, which is in line with the aforementioned hypothesis of trapped charge-driven degradation explaining the initiation of degradation on different side, depending on different charge extraction layers.

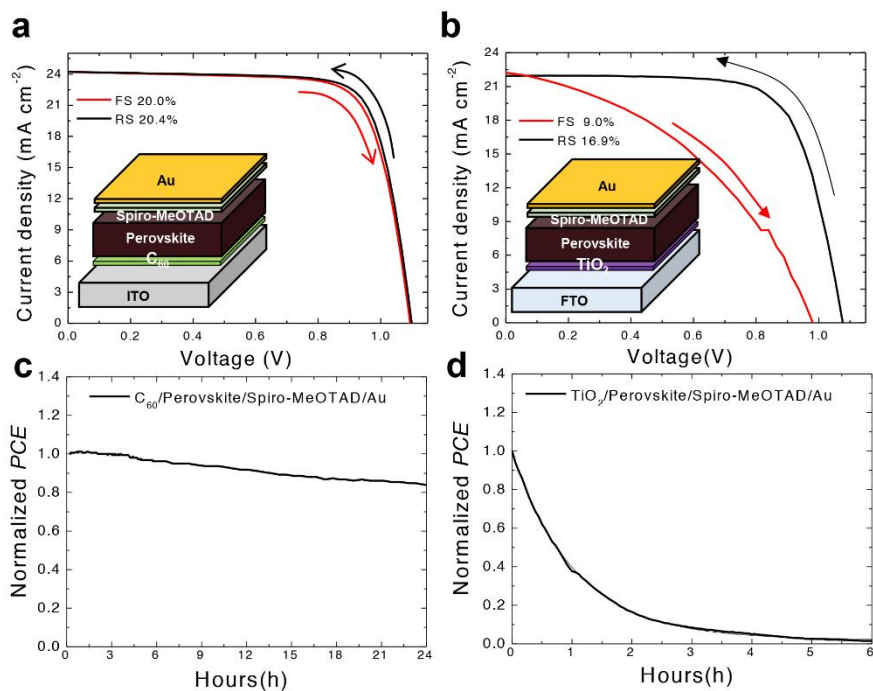


Figure 5.1 Device performance and stability depending on different ETLs. $J-V$ curves of (a) ITO/ C_{60} (35nm)/ $MA_{0.6}FA_{0.4}PbI_{2.9}Br_{0.1}$ (500nm)/Spiro-MeOTAD(250nm)/Au(50nm) and (b) FTO/ TiO_2 (40nm)/ $MA_{0.6}FA_{0.4}PbI_{2.9}Br_{0.1}$ (500nm)/Spiro-MeOTAD(250nm)/Au(50nm) measured in the reverse (black) and forward (red) scans with a 200 ms sweep delay. (c, d) Time evolution of the normalized PCE measured under one sun illumination in ambient conditions (relative humidity = 30%) of the (c) C_{60} and (d) TiO_2 based devices.

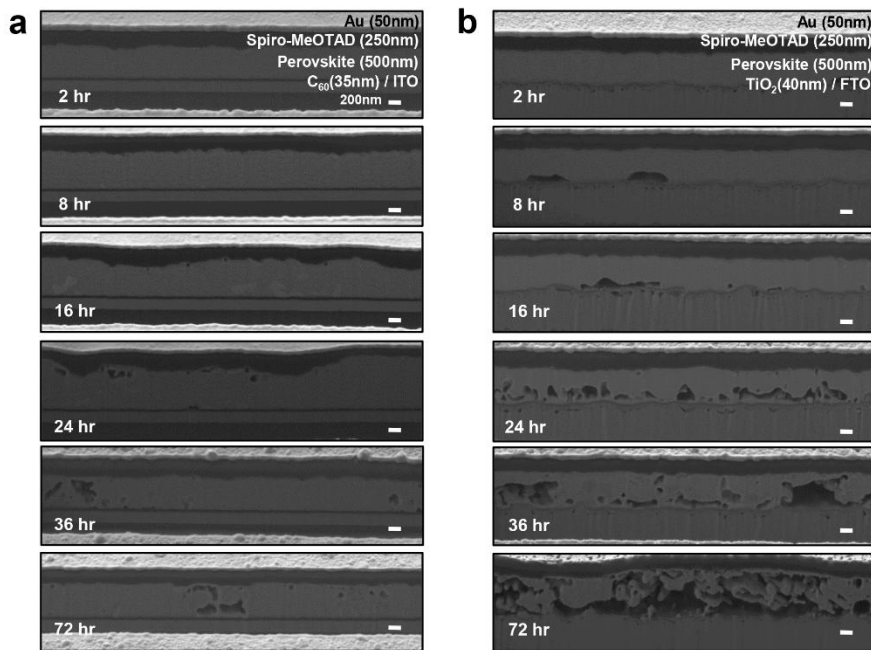


Figure 5.2 Degradation patterns depending on different ETLs. (a, b) Time evolution of the FIB-SEM cross-sectional images of the (a) C₆₀ and (b) TiO₂ based devices aged for 72 h under light illumination in ambient conditions. Scale bars = 200 nm.

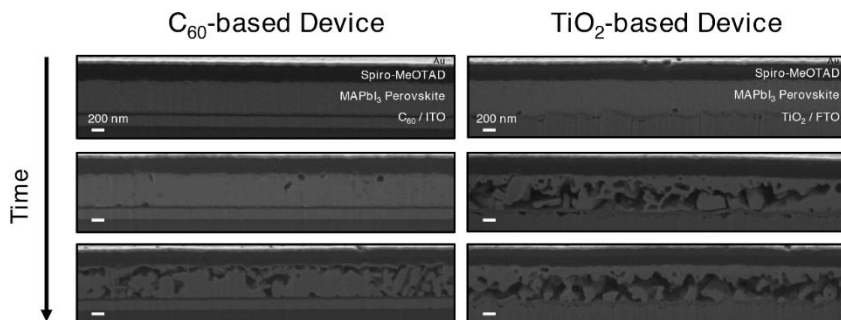


Figure 5.3 Degradation patterns of the C_{60} - (left) TiO_2 - (right) based devices employing $MAPbI_3$ perovskite, which were aged under one sun illumination in ambient conditions. Scale bars = 200 nm. As was shown in Fig. 1 for our mixed perovskite, the cell employing $MAPbI_3$ also showed the same pattern of degradation: for TiO_2 -based cell, the degradation begins from the interface between $MAPbI_3$ and TiO_2 electron extraction layer, but for C_{60} -based cell, the degradation begins from the opposite side of interface between $MAPbI_3$ and Spiro-MeOTAD hole extraction layer.

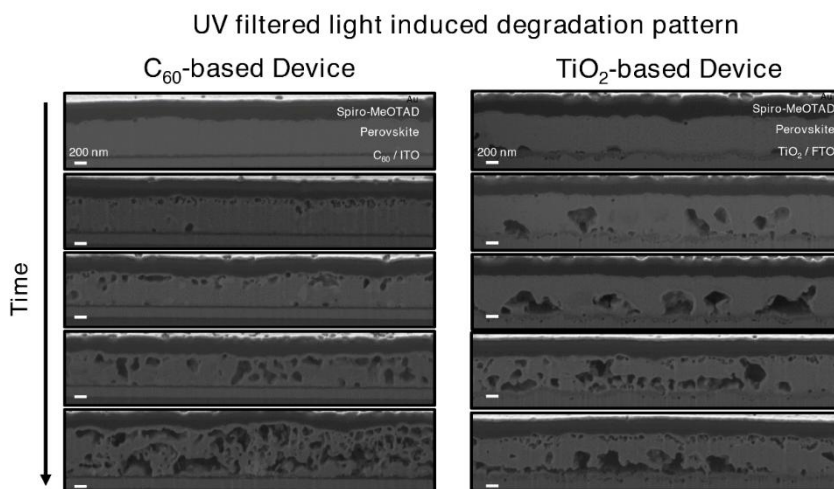


Figure 5.4 Time evolution of the FIB-SEM cross-sectional images of the C₆₀ (left) and TiO₂ (right) based devices employing MA_{0.6}FA_{0.4}PbI_{2.9}Br_{0.1} perovskites, which were aged for 48 h under UV filtered (Edmund Optics, 425nm High Performance UV Longpass Filter) light illumination in ambient conditions. Scale bars = 200 nm.

To prove this compelling hypothesis of trapped charge driven degradation, we have configured a novel experimental setup employing an ion generator by corona discharge and a stainless chamber that blocks all incident light from outside as shown in **Figure.5.5a**. Detailed descriptions of the ion generation via corona discharge method and ion deposition can be found in the references [67,68]. The air inside the chamber is isolated from the outside and controlled by two gas inlets that are connected to the independent gas sources (Gas 1 and Gas 2). Gas 1 is ionized by applying a high voltage to the pin of the corona chamber, delivered to the deposition chamber by gas flow, and deposited on the perovskite film placed at the bottom of the deposition chamber. Gas 2 passes through a water bubbler to regulate the humidity level in the deposition chamber. We measured the time evolution of the absorption spectra as the perovskite films were gradually degraded in the deposition chamber. Gas 1 was chosen as nitrogen or hydrogen for generating positive or negative ions for being used as different polarity charges trapped on the surface of perovskite, respectively while Gas 2 was nitrogen. First, we needed to check that N_2 positive ions and H_2 negative ions themselves do not affect the degradation without moisture (**Figure.5.6**). Next, we examined the degradation behavior in the presence of moisture when charged ions deposited on the surface of perovskite. When the

positively charged N_2 ions were deposited and the relative humidity in the chamber was held at 40%, the perovskite film rapidly decays as shown in **Figure 5.5b**. The deposition of negatively charged H_2 ions also showed the similar irreversible degradation behavior under the same moisture level in **Figure 5.5c**. Although **Figure 5.5c** for negative charges appears to cause slower degradation than the case shown in **Figure 5.5b** for positive charges, this could not tell which polarity charges affect more adversely on the degradation since ion generation for different polarity in our experiment is different. Note that, on the other hand, without depositing charges, the absorption spectra and XRD patterns of the perovskite film were hardly changed for 2 days even under 90% humidity as was shown in **Figure 5.7**. Similarly, at the presence of only charges without moisture, the degradation did not occur at all as shown in **Figure 5.8**. This suggests that the irreversible degradation of perovskite materials only take place when both moisture and charges exist simultaneously. Moreover, the structurally distorted (conventional) $MAPbI_3$ film was degraded more quickly than the mixed stable $MA_{0.6}FA_{0.4}PbI_{2.9}Br_{0.1}$ under the same moisture and ion deposition level (**Figure 5.8**). Based on these observations, the degradation mechanism could be thought of two-step process: the formation of hydrated perovskite by humidity and the irreversible decomposition by trapped charges. The first step of the formation of

hydrated perovskite was already reported by several groups[21,49]. Here, we suggest that local electric field caused by trapped charge could distort electrostatically the structure of hydrated perovskite in which octahedral PbX_6^{4-} interacts with both organic cation and H_2O and trigger the initiation of irreversible decomposition of perovskite. Leijtens et al.[57] found the irreversible degradation near the gold electrodes coated on perovskite film by applying a weak external field of 600 V cm^{-1} in the presence of moisture and attributed it to the ion movement through electric field. Since an electric field was applied between two electrodes touching perovskite film, electric current could flow and there was a possibility of charge trapping underneath the electrode, which might have played a role for degradation. To isolate the effect of pure external electric field, we examined the degradation of perovskite materials by applying non-contact electric field which was given by two floating electrodes; one electrode is in air above perovskite film coated on ITO glass and the other electrode exists beneath the glass. We found no degradation up to 12 kV cm^{-1} under 90 % RH (See **Figure 5.9**). Note that this field will be dropped across the air gap and therefore, the real field inside perovskite film should be different from the given field and the perovskite film might be uniformly polarized by one-directional strong E-field because perovskite materials have a high dielectric constant[19,69]. Therefore,

further study should be needed to completely understand the effect of pure external electric field. It is noted that the differences between the fields due to the trapped charges and the external field lie in the point-like character of the trapped charges, which produce locally huge and irregular fields. The huge and irregular fields formed by charges trapped along grain boundaries could help the process of deprotonation[70].

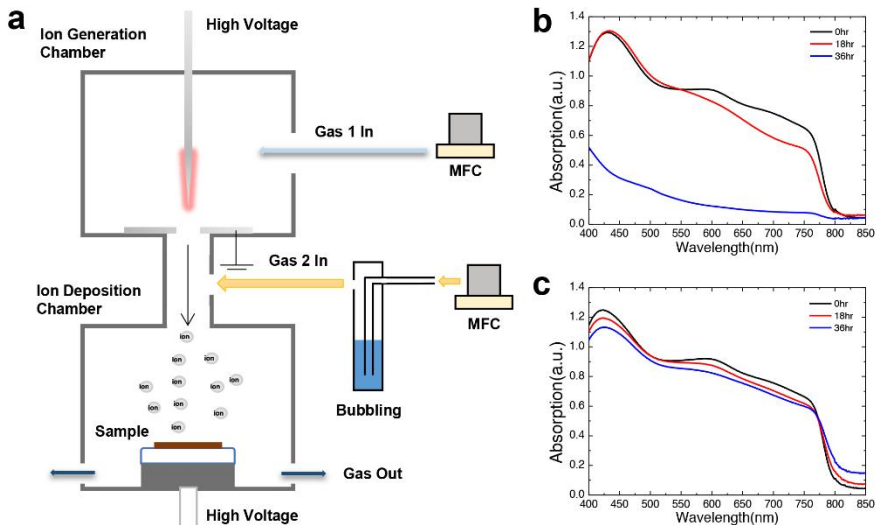


Figure 5.5 Experiments for trapped charge driven degradation.

(a) Experimental setup of corona discharge for ion generation, bubbling system for humidification, and SUS chamber for ion deposition and blocking light. Absorption spectra of the perovskite film measured at an interval of 18 hours during deposition of **(b)** positive nitrogen ions and **(c)** negative hydrogen ions at 40% relative humidity.

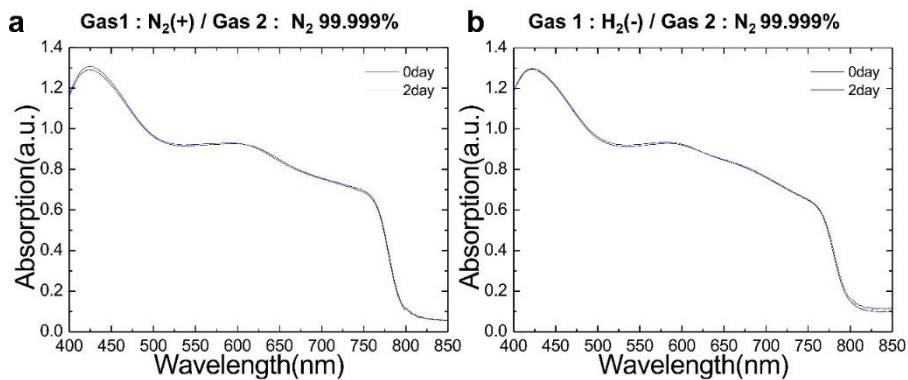


Figure 5.6 Absorption spectra of the perovskite film under (a) continuous positive nitrogen and (b) negative hydrogen ion deposition in moisture-free dark condition.

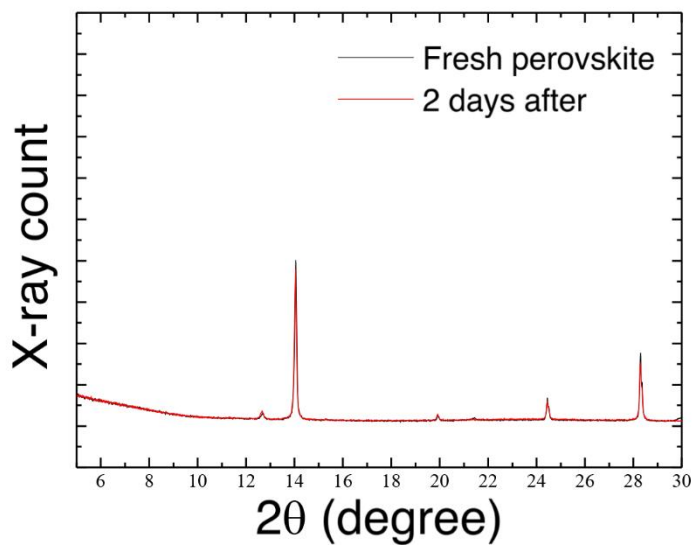


Figure 5.7 XRD patterns of the perovskite film before (red) and after (black) aged at 90% relative humidity for 2 days.

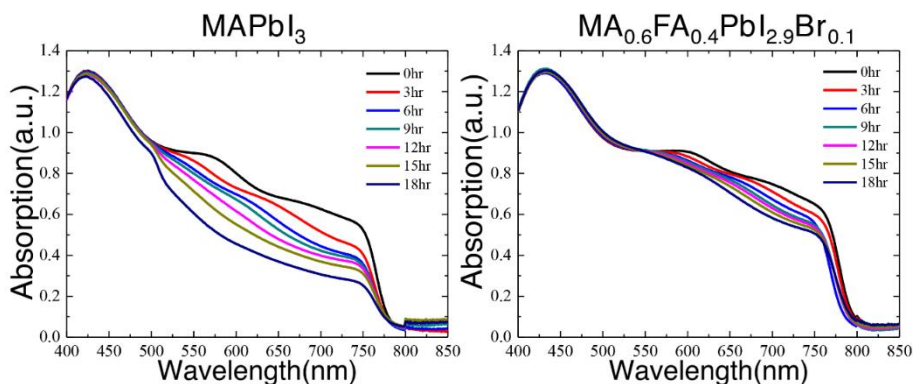


Figure 5.8 Comparison of the degradation rates of MAPbI₃ and MA_{0.6}FA_{0.4}PbI_{2.9}Br_{0.1} perovskite films at 40% relative humidity with positive nitrogen ion deposition. Absorption spectra were measured at an interval of 3 hr.

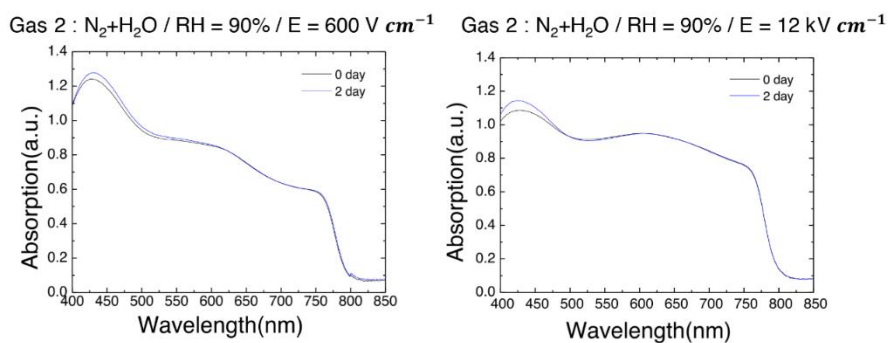


Figure 5.9 The effect of non-contact high electric field on the degradation of the perovskite film at high relative humidity (90%) under dark condition.

Next we investigated how trapped charge could decompose perovskite material in time by examining morphology evolution via SEM analysis. As shown in **Figure.5.10e-l** (Tilted top-view and cross-sectional images) and **Figure 5.11** (Top-view images), the degradation is initiated from the grain boundaries. As the reaction continues, the color of the film turns into yellow (**Figure.5.10a-d**), indicating that the perovskite is irreversibly decomposed to PbI_2 (see XRD patterns after degradation in **Figure 5.12**). It is interesting to dig into why degradation occurs from grain boundaries in line with our trapped charge mechanism. To check the distribution of trapped charges on the surface of perovskite after uniform ion deposition, we measured Kelvin Probe Force Microscopy (KPFM) of un-treated perovskite and ion-treated perovskite films. **Figure.5.10m,n** shows topology and surface potential distribution of the perovskite surface on which positive N_2^+ ions were uniformly showered. Striking coincidence between two images is the evidence that charges are preferentially trapped along grain boundaries. Overlapped image of topology and potential distribution shown in **Figure 5.13** clearly demonstrates charges are trapped along grain boundaries even though ions are showered uniformly. For untreated sample, there is no correlation between topology and potential distribution (see **Figure 5.13**). With this charge trapping along grain boundaries, experimentally observed

degradation pattern following grain boundaries and the fact that the irreversible degradation occurs only when moisture and charges exist together are the evidences that trapped charges would be responsible for the initiation of irreversible degradation of perovskite materials. It is now apparent that grain boundaries are the most vulnerable sites for the degradation because they provide charge accumulation sites as well as infiltration pathway of water vapor[17]. Successful enhancement of stability utilizing high mobility inorganic charge extraction layers supports the present idea[22,60].

To further investigate the possibility that the above mentioned intriguing experimental observation of irreversible degradation under light soaking might be related to the mechanism of trapped charges of the present study, we measured KPFM images on the surface of perovskite after light illumination without ion deposition. As shown in **Figure 5.13**, charges are clearly trapped along grain boundaries for the ITO/C₆₀/perovskite sample soaked by light, which is in agreement with the previous report³⁹. These results confirmed that light soaking alone induces charge trapping along the grain boundaries of perovskite material like was done by introduction of ion charges in the dark condition. From our concept, these trapped charges can now trigger the irreversible degradation due to moisture as the same happened when ion charges are deposited in the dark. Therefore, the

fundamental cause for irreversible degradation would be the same, that is, the trapped charges that could trigger the irreversible degradation under humid air. Such irreversible degradation under light soaking was reported in previous several reports[49], but, the reason has not been clearly elucidated so far although Christians *et al.*[49] suggested the lessened hydrogen bonding after photoexcitation as a possible cause. Here, we argue that trapped charges under moisture would be responsible for the initiation of irreversible degradation under light or in the dark since light illumination always generates charges and traps the charges along grain boundaries as shown earlier. This can explain well why moisture itself without illumination or intentional ion deposition only hydrated perovskite reversibly. Light illumination under nitrogen gas without moisture for two days was shown to hardly degrade the perovskite as shown in **Figure 5.14** which is strongly contrasted with the case of light illumination under moisture.

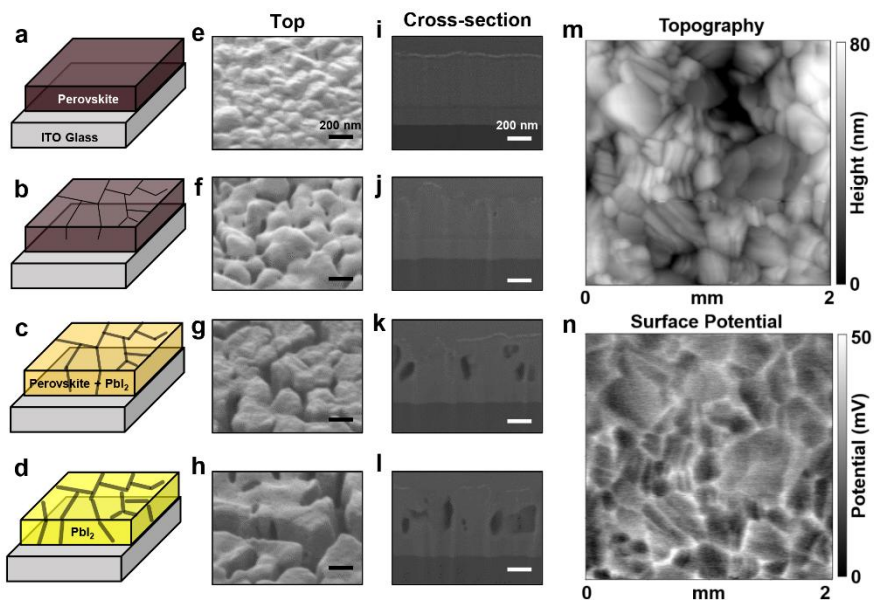


Figure 5.10 SEM and KPFM measurements. (a-d) Schematic illustration of perovskite degradation processes (left), (e-h) top-view (middle) and (i-l) cross-sectional (right) SEM images of perovskite layers (a,e,i) before, (b,f,j) after 6 hours, (c,g,k) 12 hours, and (d,h,l) 18 hours by ion deposition in humidified nitrogen. The color change from dark brown to yellow in (a,b,c,d) represents the gradual degradation process. Black lines and their widths in (a,b,c,d) represent grain boundaries and degradation extent, respectively. Scale bars = 200 nm. (m) Topography and (n) surface potential profile of $\text{MA}_{0.6}\text{FA}_{0.4}\text{PbI}_{2.9}\text{Br}_{0.1}$ film obtained from KPFM measurements after deposition of N_2 positive ions.

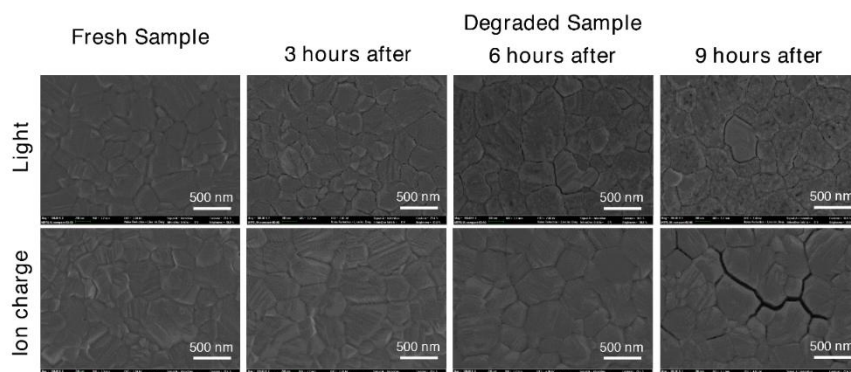


Figure 5.11 The top-view SEM images of the fresh and degraded perovskite films. The degraded samples were aged for 9 hours under one sun light illumination (first row) and ion charge deposition (second row), respectively.

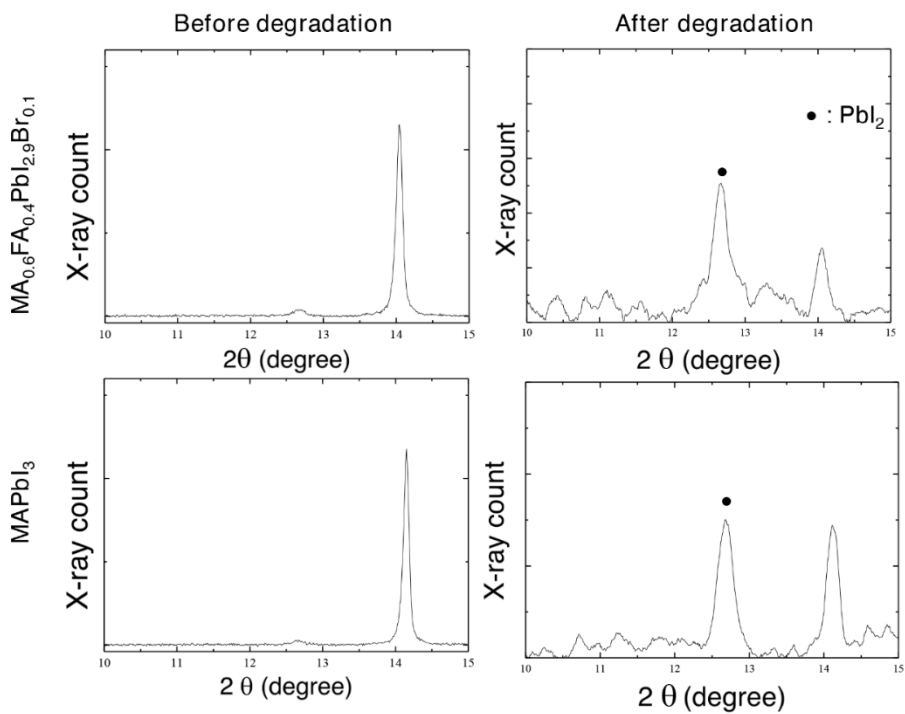


Figure 5.12 XRD patterns of the MA_{0.6}FA_{0.4}PbI_{2.9}Br_{0.1} and MAPbI₃ film before and after degradation by trapped charges in the presence of moisture.

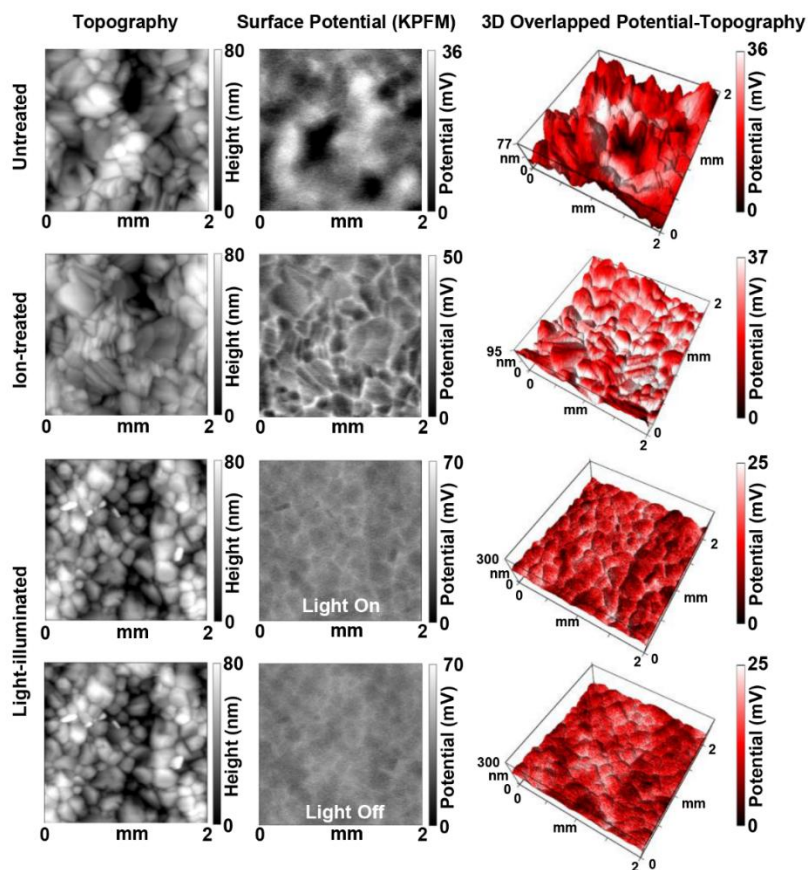


Figure 5.13 Topographies (first column) and surface charge density profiles (second column) of untreated (first row), Ion-treated (second row), and light-illuminated (third and fourth row) $\text{MA}_{0.6}\text{FA}_{0.4}\text{PbI}_{2.9}\text{Br}_{0.1}$ perovskite film. The images in the third and fourth row were obtained from light on and off during the measurement, respectively. The images in the third column show 3D plots of topographies colored based on the surface potential values. Both images of light illuminated cases show clear charge trapping along grain boundaries, but the charge trap is more contrasted when KPFM operation is under the light on.

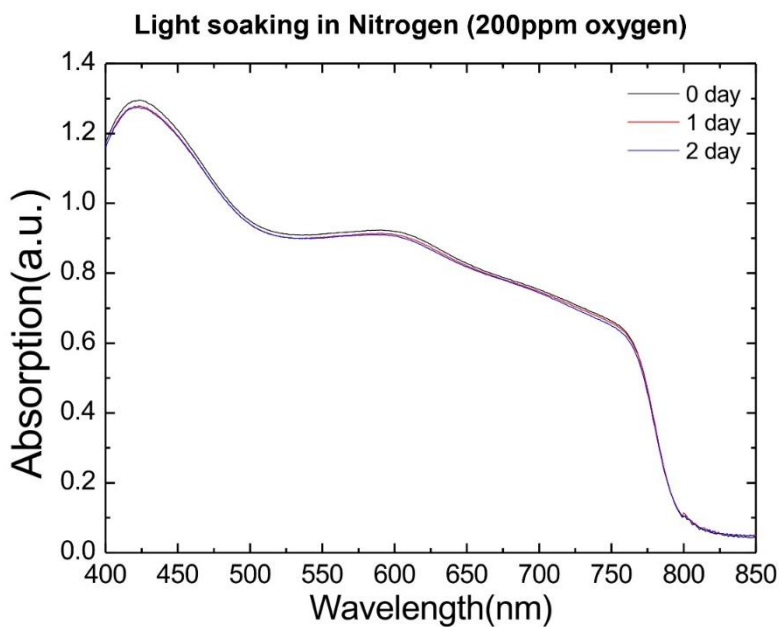
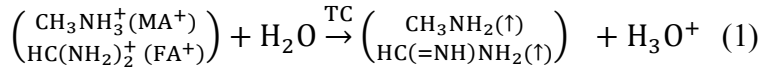
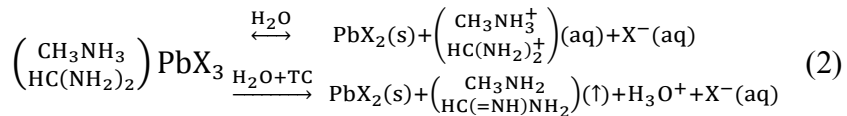


Figure 5.14 Absorption spectra of the perovskite film under one sun illumination in nitrogen. Light was illuminated in a moisture-free condition.

We suggest a possible scenario how trapped charge could trigger the irreversible decomposition of perovskite materials. First, in the presence of water molecules, perovskite materials are known to form hydrates. Within the hydrated perovskite, octahedral PbX_6^{4-} interacts with both organic cations (CH_3NH_3^+ , $\text{HC}(\text{NH}_2)_2^+$) and H_2O^{11} . Then, the charges trapped at the defect site regardless of polarity could help to deprotonate organic cations by induced local electric field like the way that was well known from the soft matter physics on electric-field induced de-protonation of organic molecules[71,72]. Such de-protonation process[62,70] in the presence of water could yield volatile molecules like CH_3NH_2 and $\text{HC}(\text{=NH})\text{NH}_2$ that can evaporate at room temperature. The following deprotonation from organic cations could take place due to trapped charge induced local electric field:



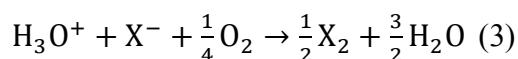
where TC means trapped charge. Evaporation of resulted volatile neutral molecules could shift the following equilibrium reaction that prevail during the formation of hydrates towards the right hand side, which causes the beginning of irreversible degradation of perovskite:



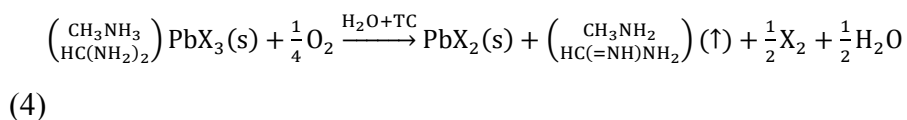
where X denotes halide. In addition, trapped charges could help the hydration process by distorting the structure of perovskite electrostatically, which leads water molecule to penetrate easily into the perovskite structure.

Next, we investigated the effect of oxygen on the moisture induced degradation of perovskite materials. Previous studies on device encapsulation have mostly focused on blocking moisture, and overlooked the effect of oxygen. However, we found an interesting result that is the synergetic effect of oxygen on the process of moisture induced degradation of perovskites. To test this, we switched the Gas 2 from N₂ to dry air (N₂+O₂:8:2) for bubbling water (**Figure 5.15a**) with the Gas 1 remaining as N₂ for ion generation. As shown in **Figure 5.15b**, the addition of oxygen under the same condition of trapped charge and moisture of RH=40% clearly showed more rapid degradation compared to the case without oxygen (**Figure 5.15a**). We also verified that degradation did not happen if a dry air gas was employed as Gas 2 without moisture (**Figure 5.16**). This implies that oxygen alone would not harm the perovskite even under the existence of trapped charges, but, the oxygen could worsen the degradation process in the presence of water and trapped charges. Previously, Niu *et al.*[73] suggested reaction equations of oxygen-involved degradation in humid air condition, which represent the formation of

H₂O as a reaction product. Similarly, we explain the fast degradation in the presence of oxygen more clearly based on the scavenging effect of oxygen on H₃O⁺ proton generated from irreversible de-protonation process, Eq(1). The process of scavenging H₃O⁺ by oxygen could be expressed as follows.



The overall chemical reaction of the oxygen involved degradation can be expressed as:



We also confirmed that solid I₂ is produced from the perovskite degraded in ambient air, which is evidenced by XRD results (see **Figure 5.17**). Interestingly, the overall reaction produces water, which is in agreement with the previous work[73], and then this water could cause a chain reaction of water induced degradation. Therefore, oxygen, which comprises about 20% of the atmosphere, should be considered as an additional target that must be avoided together with moisture.

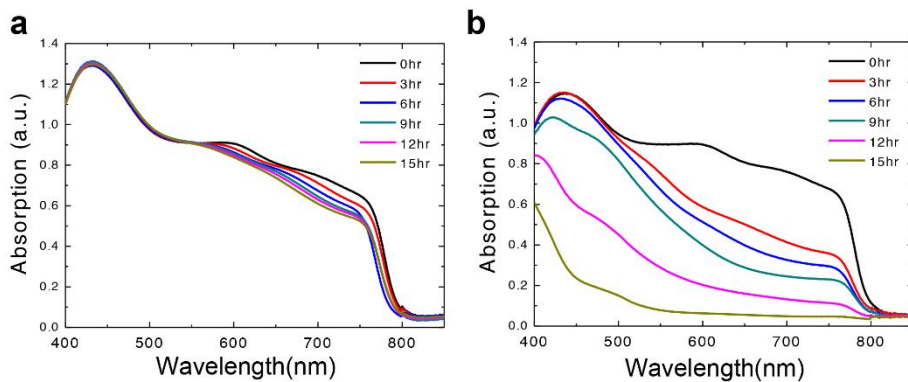


Figure 5.15 Synergetic effect of oxygen on degradation. Time evolution of the absorption spectra of $\text{MA}_{0.6}\text{FA}_{0.4}\text{PbI}_{2.9}\text{Br}_{0.1}$ films (a) in humidified nitrogen and (b) in humidified air measured at an interval of 3 hours during deposition of positive nitrogen ions. In both cases, the relative humidity is 40%.

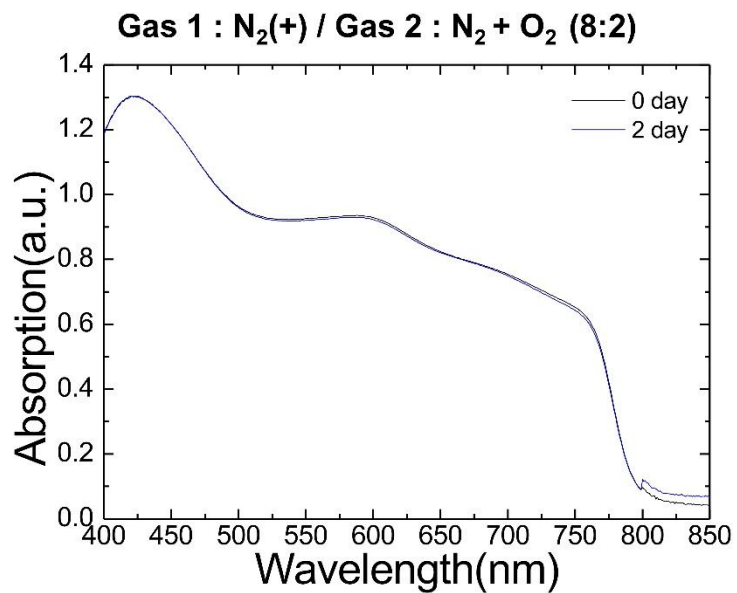


Figure 5.16 Absorption spectra of the perovskite film in dry air after deposition of positive nitrogen ions.

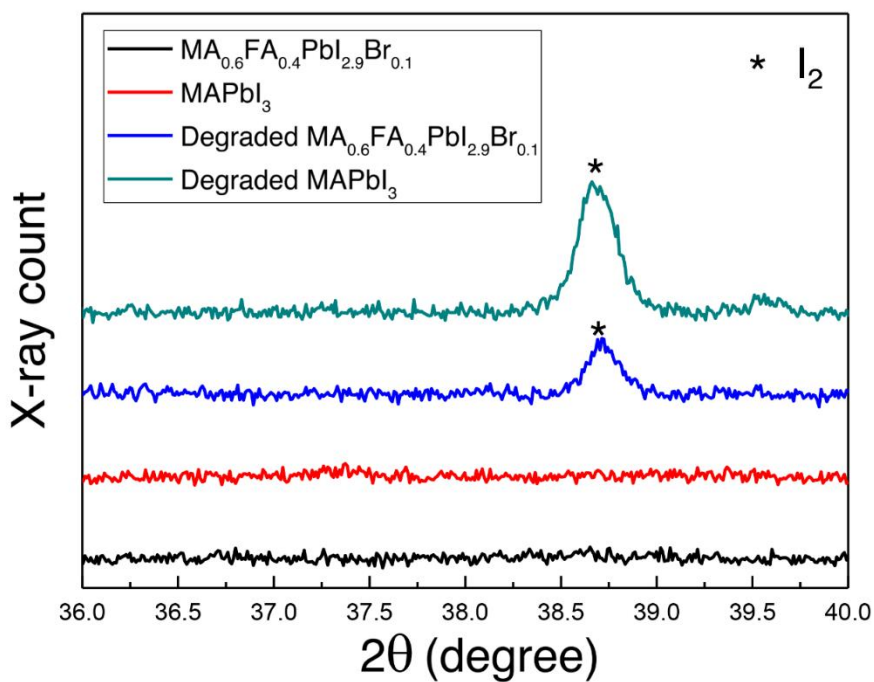


Figure 5.17 X-ray diffraction (XRD) patterns of the fresh and degraded samples of MAPbI₃ and MA_{0.6}FA_{0.4}PbI_{2.9}Br_{0.1}. The graph shows the magnified XRD patterns around the peak originating from I₂ (*).

5.3. Conclusion

We found that trapped charges would be responsible for triggering the irreversible degradation in the moisture induced degradation of perovskite materials regardless of charge polarity. To verify this, we designed a novel experimental setup enabling the deposition of different polarity charges on the surface of perovskites for controlled moisture degradation experiments. From this setup, we demonstrated that the perovskite materials degraded irreversibly along grain boundaries only when both moisture and trapped charge exist simultaneously. During the course of study, we developed and used a new mixed perovskite material that ensured both high performance and structural stability. Our study explains both why the degradation begins to occur from the different side of interface between perovskite and charge extraction layer for different charge extraction layers and how light soaking always degrades irreversibly in the presence of moisture. KPFM study reveals that charges are trapped preferentially along grain boundaries of perovskites even under uniform deposition of ion charges or uniform illumination of light, which supports our idea of trapped charge driven degradation. We also found the synergetic effect of oxygen in the process of moisture induced degradation. The present study suggests that the prevention of accumulation of charges at the interface is very important in addition to

proper encapsulation for developing commercially viable perovskite solar cells.

5.4. Experimental method

Experimental setup for ion generation and deposition

The whole chamber contains two connected chambers: the ion generation(IG) chamber and the ion deposition(ID) chamber. The IG chamber has cylindrical shape with 30 mm diameter and 35 mm height. It is made of transparent acrylic which makes it possible to see the state of corona discharge during experiment. Stainless steel pin and plate creates highly asymmetric electric field in the chamber, when a bias voltage is applied between the pin and the plate. Gas 1 can flow into the chamber through an inlet on the side wall. The polarity of generated ions is determined by the polarity of applied voltage to the pin. The current of generated ions was measured by Faradaycup electrometer (Keithley Sub-femtoamp remote sourcemeter, 6430). A high-voltage supply (FuG ElektronikGmbH, HCP140-12500) apply voltage to the pin and the substrate in the ID chamber.

The ions generated in the IG chamber flows through a 115 mm long pipe with a 1.5mm diameter that connects the IG and ID chambers. A tee tube connected to this pipe introduces Gas 2 into the system. The flow rates of Gas 1 and 2 are both controlled by mass flow controllers (MKS instruments, MFC Controller 247D, MFC 1179A). The negatively (positively) charged gas ions are electrostatically attracted and deposited on the positively (negatively) biased substrate with the bias voltage of 2kV (-2kV).

Corona ion generation

Nitrogen gas inflow with the flow rate of 2 lpm was transformed into positive nitrogen ions by applying 4.2 kV to the pin. The electric current of generated nitrogen ions was measured to be 20.6-25.8 pA, which is indicative of positive ion generation. To generate negative ions, we used hydrogen gas with the flow rate of 2 lpm and applied negative bias (-1.55 kV) to the pin, which generates the current of -3.2 ~ -4.8 pA. (see **Table 5.1**)

Atmosphere control

To maintain the condition of the air inside the chamber at constant, the flow rate of Gas 2 was controlled by MFC and set as 1.5 lpm throughout the measurements. Nitrogen, dry air, humidified nitrogen and air were used as Gas 2. Nitrogen and hydrogen gases are highly purified by 99.999%, and dry air consists of 80% of nitrogen (99.999%) and 20% of oxygen(99.995%). Gas 2 passes through a water bubbler that controls the humidity in the chamber. The relative humidity was measured by portable multifunction data-logger(Delta OHM, Data logger DO9847, Temp&Humidity probe HP474AC) at the gas exit of deposition chamber.

		Flow rate(L m ⁻¹)	Current of generated ion (pA)	Applied voltage
Gas1	Nitrogen	2	20.6 ~ 25.8	4.2kV(0.009 mA)
	Hydrogen	2	-3.2 ~ -4.8	-1.55kV(-0.4 mA)
Gas2	Nitrogen	1.5		
	Dry air	1.5	-	

Table 5.1 The parameters for ion generation and data obtained from MFC controller and Faradaycup

Topography and Kelvin probe force microscopy

All the samples for topography and Kelvin probe force microscopy measurements were prepared on ITO glass substrates. The perovskite films were spin-coated on the ITO glass and ITO/C₆₀ substrate. The ion-treated sample was prepared by depositing N₂ positive corona ion for 1 hr on the ITO/perovskite substrate. In the case of the light-illuminated sample, the ITO/C₆₀ substrate was used in order to measure positive charge accumulation profile. After one sun illumination for 1 hr, the sample was measured under light on or off during KPFM operation.

Topography and Kelvin probe force microscopy (KPFM) signals were measured by using an atomic force microscope (MFP-3D, Asylum Research, USA) with a Pt-coated tip with the spring constant of 2 nN nm⁻¹ and the resonant frequency of 77 kHz. For each line scanning, topography was first measured and successively the surface potential was measured while scanning the same line at a fixed distance above the sample surface. The tip was positioned sufficiently away from the substrate (as far as 20 nm) in order to exclude the cross-talk artefacts from topography footprints¹². The surface potential was measured using an active electronic feedback circuitry: the bias voltage to the tip was modulated in order to equate the potential of the tip with that of the surface, resulting in minimum vibration amplitude

of the AFM tip at the fundamental frequency. A 150W halogen bulb with single fiber light guide was used for illumination.

6. References

- [1] A. Kojima, K. Teshima, Y. Shirai & T. Miyasaka. "Organometal Halide Perovskites as Visible-Light Sensitizers for Photovoltaic Cells". *Journal of the American Chemical Society* **131**, 6050-6051 (2009).
- [2] H.-S. Kim *et al.* "Lead Iodide Perovskite Sensitized All-Solid-State Submicron Thin Film Mesoscopic Solar Cell with Efficiency Exceeding 9%" **2**, 591 (2012).
- [3] J. Burschka *et al.* "Sequential deposition as a route to high-performance perovskite-sensitized solar cells". *Nature* **499**, 316-319 (2013).
- [4] M. Liu, M. B. Johnston & H. J. Snaith. "Efficient planar heterojunction perovskite solar cells by vapour deposition". *Nature* **501**, 395-398 (2013).
- [5] N. J. Jeon *et al.* "Compositional engineering of perovskite materials for high-performance solar cells". *Nature* **517**, 476-480 (2015).
- [6] W. S. Yang *et al.* "High-performance photovoltaic perovskite layers fabricated through intramolecular exchange". *Science* **348**, 1234 (2015).
- [7] W. S. Yang *et al.* "Iodide management in formamidinium-lead-halide-based perovskite layers for efficient solar cells". *Science* **356**, 1376 (2017).
- [8] J.-H. Im, C.-R. Lee, J.-W. Lee, S.-W. Park & N.-G. Park. "6.5% efficient perovskite quantum-dot-sensitized solar cell". *Nanoscale* **3**, 4088-4093 (2011).
- [9] J.-H. Im, H.-S. Kim & N.-G. Park. "Morphology-photovoltaic property correlation in perovskite solar cells: One-step versus two-

- step deposition of CH₃NH₃PbI₃". *APL Materials* **2**, 081510 (2014).
- [10] J.-H. Im, I.-H. Jang, N. Pellet, M. Grätzel & N.-G. Park. "Growth of CH₃NH₃PbI₃ cuboids with controlled size for high-efficiency perovskite solar cells" **9**, 927 (2014).
- [11] N. Ahn, S. M. Kang, J.-W. Lee, M. Choi & N.-G. Park. "Thermodynamic regulation of CH₃NH₃PbI₃ crystal growth and its effect on photovoltaic performance of perovskite solar cells". *Journal of Materials Chemistry A* **3**, 19901-19906 (2015).
- [12] N. J. Jeon *et al.* "Solvent engineering for high-performance inorganic–organic hybrid perovskite solar cells" **13**, 897 (2014).
- [13] M. Xiao *et al.* "A Fast Deposition-Crystallization Procedure for Highly Efficient Lead Iodide Perovskite Thin-Film Solar Cells". *Angewandte Chemie* **126**, 10056-10061 (2014).
- [14] H. Miyamae, Y. Numahata & M. Nagata. "THE CRYSTAL STRUCTURE OF LEAD(II) IODIDE-DIMETHYLSULPHOXIDE(1/2), PbI₂(dmsO)₂". *Chemistry Letters* **9**, 663-664 (1980).
- [15] I. Wharf, T. Gramstad, R. Makhija & M. Onyszchuk. "Synthesis and vibrational spectra of some lead(II) halide adducts with O-, S-, and N-donor atom ligands". *Canadian Journal of Chemistry* **54**, 3430-3438 (1976).
- [16] N. Ahn *et al.* "Highly Reproducible Perovskite Solar Cells with Average Efficiency of 18.3% and Best Efficiency of 19.7% Fabricated via Lewis Base Adduct of Lead(II) Iodide". *Journal of the American Chemical Society* **137**, 8696-8699 (2015).
- [17] T. Leijtens *et al.* "Stability of Metal Halide Perovskite Solar Cells". *Advanced Energy Materials* **5**, 1500963-n/a (2015).
- [18] Z. Li *et al.* "Stabilizing Perovskite Structures by Tuning Tolerance Factor: Formation of Formamidinium and Cesium Lead Iodide

- Solid-State Alloys". *Chemistry of Materials* **28**, 284-292 (2016).
- [19] Q. Lin, A. Armin, R. C. R. Nagiri, P. L. Burn & P. Meredith. "Electro-optics of perovskite solar cells" **9**, 106 (2014).
- [20] N. Ahn *et al.* "Trapped charge-driven degradation of perovskite solar cells" **7**, 13422 (2016).
- [21] J. Yang, B. D. Siempelkamp, D. Liu & T. L. Kelly. "Investigation of CH₃NH₃PbI₃ Degradation Rates and Mechanisms in Controlled Humidity Environments Using in Situ Techniques". *ACS Nano* **9**, 1955-1963 (2015).
- [22] W. Chen *et al.* "Efficient and stable large-area perovskite solar cells with inorganic charge extraction layers". *Science* **350**, 944 (2015).
- [23] H.-S. Kim *et al.* "Control of I–V Hysteresis in CH₃NH₃PbI₃ Perovskite Solar Cell". *The Journal of Physical Chemistry Letters* **6**, 4633-4639 (2015).
- [24] Y. Fu *et al.* "Solution Growth of Single Crystal Methylammonium Lead Halide Perovskite Nanostructures for Optoelectronic and Photovoltaic Applications". *Journal of the American Chemical Society* **137**, 5810-5818 (2015).
- [25] N.-G. Park. "Organometal Perovskite Light Absorbers Toward a 20% Efficiency Low-Cost Solid-State Mesoscopic Solar Cell". *The Journal of Physical Chemistry Letters* **4**, 2423-2429 (2013).
- [26] H. Zhou *et al.* "Interface engineering of highly efficient perovskite solar cells". *Science* **345**, 542 (2014).
- [27] M. Grätzel. "The light and shade of perovskite solar cells" **13**, 838 (2014).
- [28] H.-S. Ko, J.-W. Lee & N.-G. Park. "15.76% efficiency perovskite solar cells prepared under high relative humidity: importance of PbI₂ morphology in two-step deposition of CH₃NH₃PbI₃". *Journal of Materials Chemistry A* **3**, 8808-8815 (2015).

- [29] S. M. Kang, N. Ahn, J.-W. Lee, M. Choi & N.-G. Park. "Water-repellent perovskite solar cell". *Journal of Materials Chemistry A* **2**, 20017-20021 (2014).
- [30] P. S. Richard. "Nucleation: theory and applications to protein solutions and colloidal suspensions". *Journal of Physics: Condensed Matter* **19**, 033101 (2007).
- [31] Y. Kawamura, H. Mashiyama & K. Hasebe. "Structural Study on Cubic–Tetragonal Transition of CH₃NH₃PbI₃". *Journal of the Physical Society of Japan* **71**, 1694-1697 (2002).
- [32] J.-W. Lee, D.-J. Seol, A.-N. Cho & N.-G. Park. "High-Efficiency Perovskite Solar Cells Based on the Black Polymorph of HC(NH₂)₂PbI₃". *Advanced Materials* **26**, 4991-4998 (2014).
- [33] J. H. Heo, H. J. Han, D. Kim, T. K. Ahn & S. H. Im. "Hysteresis-less inverted CH₃NH₃PbI₃ planar perovskite hybrid solar cells with 18.1% power conversion efficiency". *Energy & Environmental Science* **8**, 1602-1608 (2015).
- [34] G. Juška, K. Arlauskas, M. Viliūnas & J. Kočka. "Extraction Current Transients: New Method of Study of Charge Transport in Microcrystalline Silicon". *Physical Review Letters* **84**, 4946-4949 (2000).
- [35] G. Juška, N. Nekrašas, K. Genevičius, J. Stuchlik & J. Kočka. "Relaxation of photoexcited charge carrier concentration and mobility in μc-Si:H". *Thin Solid Films* **451-452**, 290-293 (2004).
- [36] A. Armin, M. Velusamy, P. L. Burn, P. Meredith & A. Pivrikas. "Injected charge extraction by linearly increasing voltage for bimolecular recombination studies in organic solar cells". *Applied Physics Letters* **101**, 083306 (2012).
- [37] G. Dennler *et al.* "Charge carrier mobility and lifetime versus composition of conjugated polymer/fullerene bulk-heterojunction

- solar cells". *Organic Electronics* **7**, 229-234 (2006).
- [38] J. A. Christians, J. S. Manser & P. V. Kamat. "Best Practices in Perovskite Solar Cell Efficiency Measurements. Avoiding the Error of Making Bad Cells Look Good". *The Journal of Physical Chemistry Letters* **6**, 852-857 (2015).
- [39] Y. Han *et al.* "Degradation observations of encapsulated planar CH₃NH₃PbI₃ perovskite solar cells at high temperatures and humidity". *Journal of Materials Chemistry A* **3**, 8139-8147 (2015).
- [40] R. Shannon. "Revised effective ionic radii and systematic studies of interatomic distances in halides and chalcogenides". *Acta Crystallographica Section A* **32**, 751-767 (1976).
- [41] A. Amat *et al.* "Cation-Induced Band-Gap Tuning in Organohalide Perovskites: Interplay of Spin–Orbit Coupling and Octahedra Tilting". *Nano Letters* **14**, 3608-3616 (2014).
- [42] B. N. Cohen, C. Labarca, N. Davidson & H. A. Lester. "Mutations in M2 alter the selectivity of the mouse nicotinic acetylcholine receptor for organic and alkali metal cations". *The Journal of General Physiology* **100**, 373 (1992).
- [43] L. Dimesso, A. Quintilla, Y. M. Kim, U. Lemmer & W. Jaegermann. "Investigation of formamidinium and guanidinium lead tri-iodide powders as precursors for solar cells". *Materials Science and Engineering: B* **204**, 27-33 (2016).
- [44] M. A. Green, A. Ho-Baillie & H. J. Snaith. "The emergence of perovskite solar cells" **8**, 506 (2014).
- [45] G. Rajendra Kumar *et al.* "Phase transition kinetics and surface binding states of methylammonium lead iodide perovskite". *Physical Chemistry Chemical Physics* **18**, 7284-7292 (2016).
- [46] Y. Wang *et al.* "Density functional theory analysis of structural and electronic properties of orthorhombic perovskite

- CH₃NH₃PbI₃".*Physical Chemistry Chemical Physics* **16**, 1424-1429 (2014).
- [47] C. C. Stoumpos, C. D. Malliakas & M. G. Kanatzidis. "Semiconducting Tin and Lead Iodide Perovskites with Organic Cations: Phase Transitions, High Mobilities, and Near-Infrared Photoluminescent Properties".*Inorganic Chemistry* **52**, 9019-9038 (2013).
- [48] J.-W. Lee *et al.* "Formamidinium and Cesium Hybridization for Photo- and Moisture-Stable Perovskite Solar Cell".*Advanced Energy Materials* **5**, 1501310-n/a (2015).
- [49] J. A. Christians, P. A. Miranda Herrera & P. V. Kamat. "Transformation of the Excited State and Photovoltaic Efficiency of CH₃NH₃PbI₃ Perovskite upon Controlled Exposure to Humidified Air".*Journal of the American Chemical Society* **137**, 1530-1538 (2015).
- [50] A. M. A. Leguy *et al.* "Reversible Hydration of CH₃NH₃PbI₃ in Films, Single Crystals, and Solar Cells".*Chemistry of Materials* **27**, 3397-3407 (2015).
- [51] S. N. Habisreutinger *et al.* "Carbon Nanotube/Polymer Composites as a Highly Stable Hole Collection Layer in Perovskite Solar Cells".*Nano Letters* **14**, 5561-5568 (2014).
- [52] H. Yoon, S. M. Kang, J.-K. Lee & M. Choi. "Hysteresis-free low-temperature-processed planar perovskite solar cells with 19.1% efficiency".*Energy & Environmental Science* **9**, 2262-2266 (2016).
- [53] D. Bi *et al.* "Efficient luminescent solar cells based on tailored mixed-cation perovskites".*Science Advances* **2** (2016).
- [54] B. J. Kim *et al.* "Highly efficient and bending durable perovskite solar cells: toward a wearable power source".*Energy & Environmental Science* **8**, 916-921 (2015).

- [55] H. Sung *et al.* "Transparent Conductive Oxide-Free Graphene-Based Perovskite Solar Cells with over 17% Efficiency". *Advanced Energy Materials* **6**, 1501873-n/a (2016).
- [56] C.-J. Tong *et al.* "Uncovering the Veil of the Degradation in Perovskite CH₃NH₃PbI₃ upon Humidity Exposure: A First-Principles Study". *The Journal of Physical Chemistry Letters* **6**, 3289-3295 (2015).
- [57] T. Leijtens *et al.* "Mapping Electric Field-Induced Switchable Poling and Structural Degradation in Hybrid Lead Halide Perovskite Thin Films". *Advanced Energy Materials* **5**, 1500962-n/a (2015).
- [58] G. Divitini *et al.* "In situ observation of heat-induced degradation of perovskite solar cells" **1**, 15012 (2016).
- [59] K. Wojciechowski *et al.* "C60 as an Efficient n-Type Compact Layer in Perovskite Solar Cells". *The Journal of Physical Chemistry Letters* **6**, 2399-2405 (2015).
- [60] J. You *et al.* "Improved air stability of perovskite solar cells via solution-processed metal oxide transport layers" **11**, 75 (2015).
- [61] A. Mei *et al.* "A hole-conductor-free, fully printable mesoscopic perovskite solar cell with high stability". *Science* **345**, 295 (2014).
- [62] S. Ito, S. Tanaka, K. Manabe & H. Nishino. "Effects of Surface Blocking Layer of Sb₂S₃ on Nanocrystalline TiO₂ for CH₃NH₃PbI₃ Perovskite Solar Cells". *The Journal of Physical Chemistry C* **118**, 16995-17000 (2014).
- [63] B. Chen, M. Yang, S. Priya & K. Zhu. "Origin of J–V Hysteresis in Perovskite Solar Cells". *The Journal of Physical Chemistry Letters* **7**, 905-917 (2016).
- [64] W. Tress *et al.* "Understanding the rate-dependent J-V hysteresis, slow time component, and aging in CH₃NH₃PbI₃ perovskite solar cells: the role of a compensated electric field". *Energy &*

- Environmental Science* **8**, 995-1004 (2015).
- [65] L. Schmidt-Mende & M. Grätzel. "TiO₂ pore-filling and its effect on the efficiency of solid-state dye-sensitized solar cells". *Thin Solid Films* **500**, 296-301 (2006).
- [66] P.-W. Liang, C.-C. Chueh, S. T. Williams & A. K. Y. Jen. "Roles of Fullerene-Based Interlayers in Enhancing the Performance of Organometal Perovskite Thin-Film Solar Cells". *Advanced Energy Materials* **5**, 1402321-n/a (2015).
- [67] H. Kim *et al.* **1**, 117 (2006).
- [68] H. Lee *et al.* "Three-Dimensional Assembly of Nanoparticles from Charged Aerosols". *Nano Letters* **11**, 119-124 (2011).
- [69] E. J. Juarez-Perez *et al.* "Photoinduced Giant Dielectric Constant in Lead Halide Perovskite Solar Cells". *The Journal of Physical Chemistry Letters* **5**, 2390-2394 (2014).
- [70] J. M. Frost *et al.* "Atomistic Origins of High-Performance in Hybrid Halide Perovskite Solar Cells". *Nano Letters* **14**, 2584-2590 (2014).
- [71] H. S. White, J. D. Peterson, Q. Cui & K. J. Stevenson. "Voltammetric Measurement of Interfacial Acid/Base Reactions". *The Journal of Physical Chemistry B* **102**, 2930-2934 (1998).
- [72] X. Zhao, S. Ong, H. Wang & K. B. Eisenthal. "New method for determination of surface pK_a using second harmonic generation". *Chemical Physics Letters* **214**, 203-207 (1993).
- [73] G. Niu *et al.* "Study on the stability of CH₃NH₃PbI₃ films and the effect of post-modification by aluminum oxide in all-solid-state hybrid solar cells". *Journal of Materials Chemistry A* **2**, 705-710 (2014).

고효율 및 고안정성 태양전지 개발을 위한 페로브스카이트 결정 형성 및 분해 연구

서울대학교 대학원 기계항공공학부

안 남 영

요약

금속 할로겐화물과 유기 할로겐화물의 화학 반응으로 쉽게 형성 할 수 있는 유기 무기 하이브리드 페로브스카이트 결정은 밴드 갭, 흡수 계수 및 캐리어 확산 길이와 같은 우수한 광전자 특성을 보인다. 이러한 특성은 페로브스카이트 결정 박막의 포괄적인 품질에 따라 변하는데, 결과적으로 최종 디바이스의 성능을 결정하게 된다. 고성능 페로브스카이트 태양 전지를 실현하기 위해서는 결정 형성의 원리를 이해하고, 기본 원리에 입각하여 페로브스카이트 결정 클러스터 박막의 제조 공정 개발을 필요로 한다. 또한, 페로브스카이트는 유기물과 무기물의 결합이 약하기 때문에, 광 조사에 의해 공기 중에서 페로브스카이트의 분해가 활발히 일어난다. 페로브스카이트 태양 전지를 수 년 동안 안정적으로 작동시키기 위해서는 페로브스카이트 분해의 근본 원인과 원리를 우선적으로 조사해야한다.

첫째, 페로브스카이트 막을 제조하는 일반적인 방법은 용액에 용해된 유기 할로겐화물과 고체상태의 납 할로겐 박막을 반응시키는 것이다. 이 **two-step** 방법이라고 하는 이 결정화 공정에서는 다양한 반응 조건이 결정 성장 속도 및 결정 크기에 영향을 미치므로 결과적으로 페로브스카이트 막의 품질이 결정된다. 고품질의

페로브스카이트 박막을 얻기 위해, 유기 할로겐화물의 온도 및 농도와 같은 여러 반응 조건들이 페로브스카이트 박막 형성에 미치는 영향을 이론적으로 예측하고, 실험적으로 조사되었다. 페로브스카이트의 결정화에 대한 열역학적 분석에 기초하여 결정 크기 방정식이 깃스 자유 에너지의 변화를 고려하여 유도되었다. 이 식으로부터, 페로브스카이트의 입자 크기는 유기 할라이드 농도 뿐만 아니라 결정화 공정의 반응 온도에 의해서도 조절 될 수 있다. 반응 온도를 -10 °C에서 50 °C로 변화시킴으로써 동일한 농도에서 입자 크기가 수 백 나노 미터에서 수 마이크로 미터로 급격히 증가하였다. 결과적으로, 농도와 온도는 페로브스카이트 입자 크기와 성능을 결정하는 데 중요한 역할을 하는 것으로 밝혀졌다. 하지만, **Two-step** 방법에서는 수직 방향의 결정 성장으로 인한 페로브스카이트 커버리지 면적의 한계가 있다.

페로브스카이트 박막의 커버리지는 광전지 성능에서 결정적이기 때문에, 페로브스카이트 결정화를 제어함으로써 완전히 덮힌 고밀도의 균질한 페로브스카이트 박막을 형성 할 수 있는 새로운 제조 방법을 개발할 필요가 있다. 페로브스카이트 박막의 형성 전에 투명한 루이스 염기 첨가화합물 박막이 중간 단계로서 형성하고, 가열을 통해 루이스 염기를 제거함으로써 서서히 결정화시켜 페로브스카이트 박막을 형성하는 것이 가능하다. 루이스 염기 첨가화합물로부터 제조된 페로브스카이트는 높은 전하 추출 특성 및 느린 재조합 속도를 나타냈다. 루이스 염기 부가 반응을 통해 제조된 페로브스카이트 태양 전지는 41 셀에서 19.7 %의 양호한 PCE 및 18.3 %의 평균 PCE를 나타내었으며, 높은 재현성을 보여주고 있다.

유무기 복합 페로브스카이트 재료는 습도 및 빛에 의한 열화에 취약하다. 가장 널리 사용되는 페로브스카이트인 $\text{CH}_3\text{NH}_3\text{PbI}_3$ (MAPbI_3)은 이온 사이의 이온 크기의 불균형 때문에 구조적으로 왜곡이 생긴 정방 결정이다. 페로브스카이트의 결정 구조는 서로 다른 이온 크기를 갖는 다른 유기 양이온 및 할라이드 음이온을 첨가하여 골드슈미트 (goldschmidt) 내성 인자를 1에 가깝게 증가 시킴으로써 보다 안정해질 수 있다. Formamidinium ($\text{HC}(\text{NH}_2)_2$) 양이온과 브로마이드 (Br) 음이온의 첨가는 입방 결정을 유도함으로써 페로브스카이트 물질을 구조적으로 안정화 시킬 뿐만 아니라 광전지 성능을 향상시킨다. $\text{MA}_x\text{FA}_{1-x}\text{PbI}_y\text{Br}_{3-y}$ 의 혼합 양이온 및 할라이드 음이온 시스템을 안정성 및 성능 면에서 종합적으로 최적화함으로써, 루이스 염기 첨가화합물 방법을 통해 형성된 구조적으로 안정화 된 혼합 조성 $\text{MA}_{0.6}\text{FA}_{0.4}\text{PbI}_{2.9}\text{Br}_{0.1}$ 페로브스카이트 태양전지는 향상된 안정성 및 최고 효율 20.2 % 나타냈다.

페로브스카이트 (Perovskite) 태양 전지는 봉지 기술을 통해 외부 공기를 차단했음에도 불구하고 실제 작동 조건하에서 빠른 분해를 나타내었는데, 그 이유는 아직 밝혀지지 않았다. 페로브스카이트 표면에 코로나 방전기를 통해 생성된 전하를 주입하기 위한 새로운 실험 장치는 페로브스카이트 표면이 전하가 포획되었을 때만 수분 존재 하에서 그레인 바운더리를 통해 비가역적으로 분해됨을 보여준다. 이 결과는 수분에 의해 유발 된 페로브스카이트 물질의 비가역적 분해가 포획된 전하에 의해 유발된다는 것을 나타낸다. Kelvin Probe Force Microscopy 측정은 가스 이온이 도포되거나, 빛이 입사되어 전하가 발생했을 때 입자 경계에서 전하가 우선적으로 갇히게 된다는 것을 확인하였다. 또한, 갇힌 전하에 의한 구동 저하에 대한 산소의

시너지 효과 또한 확인되었다. 이러한 관찰로부터, 분해 메커니즘에 대한 가능한 시나리오가 제시된다. 갇힌 전하로 인한 국지적으로 강화된 정전기력에 의해 유도된 유기 양이온의 탈 양성화는 페로브스카이트 물질의 비가 역적 분해에 기인할 것으로 예상된다.

주요어: 페로브스카이트 태양 전지, 깃스 자유 에너지, 입자 크기 방정식, 루이스 염기 부가물, 틀레랑스 인자, 입방 구조, 혼합 조성 페로브 스카이트, 분해 메커니즘, 갇힌 전하

학번: 2013-23832

List of Publications

- [1] S. M. Kang, **N. Ahn**, J.-W. Lee, M. Choi*, N.-G. Park* “Water-repellent perovskite solar cell” *Journal of Materials Chemistry A*, 2(47), 20017-20021 (2014),
- [2] J.-W. Lee, S. H. Lee, H.-S. Ko, J. Kwon, J. H. Park, S. M. Kang, **N. Ahn**, M. Choi, J. K. Kim*, N.-G. Park* “Opto-electronic properties of TiO₂ nanohelices with embedded HC(NH₂)₂PbI₃ perovskite solar cells” *Journal of Materials Chemistry A*, 3, 9179-9186 (2015)
- [3] **N. Ahn**⁺, D.-Y. Son⁺, I.-H. Jang, S. M. Kang, M. Choi*, N.-G. Park* “Highly Reproducible Perovskite Solar Cells with Average Efficiency of 18.3% and Best Efficiency of 19.7% Fabricated via Lewis Base Adduct of Lead(II) Iodide” *Journal of American Chemical Society*, 137(27), 8698-8699, (2015),
- [4] **N. Ahn**⁺, S. M. Kang⁺, J.-W. Lee, M. Choi*, N.-G. Park* “Thermodynamic regulation of CH₃NH₃PbI₃ crystal growth and its effect on photovoltaic performance of perovskite solar cells” *Journal of Materials Chemistry A*, 3(39), 19901-19906, (2015)
- [5] H. Sung⁺, **N. Ahn**⁺, M. S. Jang, J.-K. Lee, H. Yoon, N.-G. Park, M. Choi* “Transparent Conductive Oxide-Free Graphene-Based Perovskite Solar Cells with over 17% Efficiency” *Advanced Energy Materials*, 6(3), (2015)
- [6] H.-S. Kim, I.-H. Jang, **N. Ahn**, M. Choi, A. Guerrero, J. Bisquert, N.-G. Park* “Control of I–V Hysteresis in CH₃NH₃PbI₃ Perovskite Solar Cell” *Journal of Physical Chemistry Letters*, 6(22), (2016)

- [7] D.-Y. Son⁺, J.-W. Lee⁺, Y. J. Choi, I.-H. Jang, S. Lee, P. J. Yoo, H. Shin*, **N. Ahn**, M. Choi, D. Kim*, N.-G. Park*“Self-formed grain boundary healing layer for highly efficient CH₃ NH₃ PbI₃ perovskite solar cells” *Nature Energy*, 1, 16081 (2016)
- [8] **N. Ahn**⁺, K. Kwak⁺, M. S. Jang, H. Yoon, B. Y. Lee, J.-K Lee, P. V. Pikhitsa, J. Byun, M. Choi*“Trapped charge driven degradation of perovskite solar cells” *Nature Communications*, 7, 13422, (2016)
- [9] J. Yoon⁺, H. Sung⁺, G. Lee, W. Cho, **N. Ahn**, H. S. Jung*, M. Choi*“Super Flexible, High-efficiency Perovskite Solar Cells Employing Graphene Electrodes: Toward Future Foldable Power Sources” *Energy & Environmental Science*, 10, 1, (2017)
- [10] S. C. Hong⁺, G. Lee⁺, K. Ha⁺, J. Yoon, **N. Ahn**, W. Cho, M. Park, M. Choi* “Precise Morphology Control and Continuous Fabrication of Perovskite Solar Cells Using Droplet-Controllable Electro spray Coating System” *ACS Applied Materials & Interfaces*, 9, 9, (2017)
- [11] I. Jeon⁺, J. Yoon⁺, **N. Ahn**, M. Atwa, C. Delacou, A. Ansimov, E. Kauppinen, M. Choi*, S. Maruyama*, Y. Matsuo*“Carbon Nanotubes versus Graphene as Flexible Transparent Electrodes in Inverted Perovskite Solar Cells” *Journal of Physical Chemistry Letters*, 8(21), (2017)
- [12] **N. Ahn**⁺, I. Jeon⁺, J. Yoon, E. Kauppinen, Y. Matsuo*, S. Maruyama*, M. Choi*, S. Maruyama*, Y. Matsuo* “Carbon-sandwiched perovskite solar cell” *Journal of Materials Chemistry A*, DOI: 10.1039/c7ta09174e, (2017)